

# NAVAL POSTGRADUATE SCHOOL

## Monterey, California



NUMERICAL SIMULATION OF AIR  
FLOW OVER MOUNTAINS

by

John Lawrence Hayes

R. T. Williams

April 1977

Technical Report Period: July 1976 - March 1977

Approved for public release; distribution unlimited.

pared for: Naval Environmental Prediction Research Facility  
and Fleet Numerical Weather Central, Monterey, California

NAVAL POSTGRADUATE SCHOOL  
Monterey, California

Rear Admiral Isham W. Linder  
Superintendent

Jack R. Borsting  
Provost

ABSTRACT

The nature of the interaction of atmospheric flow with a mountain range of finite length is investigated. An inviscid, adiabatic primitive equation model is used to simulate steady, vertically-unsheared flow past a mountain range; various cases of mountain height and width are analyzed. A similar model for two-dimensional Boussinesq flow past a mountain on an f-plane is solved analytically following Merkine (1975) for comparison to the numerical solution. Results indicate that the atmospheric response is quite similar to that observed in the Boussinesq model. Ridging over the mountains and responses which damp in the vertical are observed in both models. Differences are noted in the magnitude of the response in the vicinity of the mountains and in the position of the downstream trough. In addition, the effect of finite difference model grid resolution is investigated by comparing simulations based on differing horizontal and vertical resolution. Results indicate that for larger scale mountains, the effect of poorer horizontal resolution is significant; vertical resolution, however, is relatively unimportant. As the horizontal scale of the mountains is reduced, vertical resolution becomes increasingly more important so that the effects of both horizontal and vertical resolution are significant.

## Unclassified

SECURITY CLASSIFICATION OF THIS PAGE (When Data Entered)

## REPORT DOCUMENTATION PAGE

READ INSTRUCTIONS  
BEFORE COMPLETING FORM

|   |                       |   |
|---|-----------------------|---|
| 1. REPORT NUMBER<br>NPS-63Wu7741  | 2. GOVT ACCESSION NO. | 3. RECIPIENT'S CATALOG NUMBER   |
| 4. TITLE (and Subtitle)<br>Numerical Simulation of Air Flow over Mountains  |                       | 5. TYPE OF REPORT & PERIOD COVERED<br>Technical Report Period<br>July 1976 - March 1977 |
|   |                       | 6. PERFORMING ORG. REPORT NUMBER  |
| 7. AUTHOR(s)<br>J. L. Hayes and R. T. Williams  |                       | 8. CONTRACT OR GRANT NUMBER(s)  |
| 9. PERFORMING ORGANIZATION NAME AND ADDRESS<br>Naval Postgraduate School<br>Monterey, California 93940  |                       | 10. PROGRAM ELEMENT, PROJECT, TASK AREA & WORK UNIT NUMBERS                             |
| 11. CONTROLLING OFFICE NAME AND ADDRESS<br>Naval Environmental Prediction Research<br>Facility and Fleet Numerical Weather Central,<br>Monterey, CA 93940   |                       | 12. REPORT DATE<br>April 1977   |
| 14. MONITORING AGENCY NAME & ADDRESS (if different from Controlling Office)   |                       | 13. NUMBER OF PAGES<br>68   |
|   |                       | 15. SECURITY CLASS. (of this report)<br>Unclassified                                    |
|   |                       | 16a. DECLASSIFICATION/DOWNGRADING SCHEDULE  |
| 16. DISTRIBUTION STATEMENT (of this Report)<br><br>Approved for public release; distribution unlimited.   |                       |   |
| 17. DISTRIBUTION STATEMENT (of the abstract entered in Block 20, if different from Report)  |                       |   |
| 18. SUPPLEMENTARY NOTES   |                       |   |
| 19. KEY WORDS (Continue on reverse side if necessary and identify by block number)<br>Numerical weather prediction<br>Flow over mountains   |                       |   |
| 20. ABSTRACT (Continue on reverse side if necessary and identify by block number)<br><br>The nature of the interaction of atmospheric flow with a mountain range of finite length is investigated. An inviscid, adiabatic primitive equation model is used to simulate steady, vertically-unsheared flow past a mountain range; various cases of mountain height and width are analyzed. A similar model for two-dimensional Boussinesq flow past a mountain on an f-plane is solved analytically following Merkine |                       |   |

Unclassified

SECURITY CLASSIFICATION OF THIS PAGE(When Data Entered)

(1975) for comparison to the numerical solution. Results indicate that the atmospheric response is quite similar to that observed in the Boussinesq model. Ridging over the mountains and responses which damp in the vertical are observed in both models. Differences are noted in the magnitude of the response in the vicinity of the mountains and in the position of the downstream trough. In addition, the effect of finite difference model grid resolution is investigated by comparing simulations based on differing horizontal and vertical resolution. Results indicate that for larger scale mountains, the effect of poorer horizontal resolution is significant; vertical resolution, however, is relatively unimportant. As the horizontal scale of the mountains is reduced, vertical resolution becomes increasingly more important so that the effects of both horizontal and vertical resolution are significant.

Unclassified

SECURITY CLASSIFICATION OF THIS PAGE(When Data Entered)

## ABSTRACT

The nature of the interaction of atmospheric flow with a mountain range of finite length is investigated. An inviscid, adiabatic primitive equation model is used to simulate steady, vertically-unsheared flow past a mountain range; various cases of mountain height and width are analyzed. A similar model for two-dimensional Boussinesq flow past a mountain on an f-plane is solved analytically following Merkine (1975) for comparison to the numerical solution. Results indicate that the atmospheric response is quite similar to that observed in the Boussinesq model. Ridging over the mountains and responses which damp in the vertical are observed in both models. Differences are noted in the magnitude of the response in the vicinity of the mountains and in the position of the downstream trough. In addition, the effect of finite difference model grid resolution is investigated by comparing simulations based on differing horizontal and vertical resolution. Results indicate that for larger scale mountains, the effect of poorer horizontal resolution is significant; vertical resolution, however, is relatively unimportant. As the horizontal scale of the mountains is reduced, vertical resolution becomes increasingly more important so that the effects of both horizontal and vertical resolution are significant.

## TABLE OF CONTENTS

|                           |  |    |
|---------------------------|--|----|
| I.                        | INTRODUCTION                                       | 11 |
| II.                       | DESCRIPTION OF MODEL AND INITIALIZATION PROCEDURES | 13 |
| A.                        | MODEL DESCRIPTION                                  | 13 |
| B.                        | ANALYTIC INITIALIZATION                            | 16 |
| C.                        | INTRODUCTION OF TOPOGRAPHY INTO THE MODEL          | 17 |
| III.                      | ANALYTIC INVESTIGATION                             | 18 |
| IV.                       | NUMERICAL RESULTS                                  | 26 |
| A.                        | BROAD MOUNTAIN RANGE CASE                          | 26 |
| 1.                        | Six-Layer Fine Resolution Model Results            | 26 |
| 2.                        | Two-Layer Fine Resolution Model Results            | 28 |
| 3.                        | Coarse Resolution Model Results                    | 28 |
| B.                        | NARROW MOUNTAIN RANGE CASE                         | 29 |
| 1.                        | Six-Layer Fine Resolution Model Results            | 29 |
| 2.                        | Two-Layer Fine Resolution Model Results            | 31 |
| V.                        | CONCLUSIONS  | 33 |
| LIST OF REFERENCES        |  | 62 |
| INITIAL DISTRIBUTION LIST |  | 63 |

## LIST OF FIGURES

|     |  |    |
|-----|--|----|
| 1.  | Sigma coordinate system and vertical distribution<br>of variables in the numerical model   | 36 |
| 2.  | Horizontal distribution of variables   | 37 |
| 3.  | Time variation of the surface pressure tendency<br>from a grid point in the vicinity of the mountains  | 38 |
| 4.  | Cross section of the topography  | 39 |
| 5.  | $9^\circ \times 1.5$ km mountain case. Analytic v profiles<br>for $\sigma = 1.0$ : 30 point vs. 60 point grid  | 40 |
| 6.  | $3^\circ \times 1.5$ km mountain case. Analytic v profiles<br>for $\sigma = 1.0$ : 30 point vs. 60 point grid  | 41 |
| 7.  | $3^\circ \times 1.5$ km mountain case. Analytic v profiles<br>for $\sigma = 0.0$ : 30 point vs. 60 point grid  | 42 |
| 8.  | $9^\circ \times 1.5$ km mountain case. Analytic v profiles<br>for $\sigma = 1.0$ vs. $\sigma = 0.0$  | 43 |
| 9.  | Analytic v profiles for $\sigma = 1.0$ : $9^\circ \times 1.5$ km<br>mountain case vs. $9^\circ \times 3.0$ km case   | 44 |
| 10. | $9^\circ \times 1.5$ km mountain range case. Six-layer fine<br>resolution model streamlines for $\sigma = .91667$  | 45 |
| 11. | $9^\circ \times 1.5$ km mountain range case. Six-layer fine<br>resolution model streamlines for $\sigma = .08333$  | 46 |
| 12. | $9^\circ \times 1.5$ km mountain range case. Analytic v<br>profile for $\sigma = 1.0$ vs. six-layer fine resolution<br>model $\sigma$ -profile for $\sigma = .91667$ | 47 |
| 13. | $9^\circ \times 1.5$ km mountain range case. Six-layer fine<br>resolution model v profiles for $\sigma = .25$ ,<br>$\sigma = .58333$ , and $\sigma = .91667$         | 48 |
| 14. | $9^\circ \times 1.5$ km mountain range case. Analytic v<br>profile for $\sigma = 0.0$ vs. six-layer fine resolution<br>model v profile for $\sigma = .08333$         | 49 |
| 15. | $9^\circ \times 1.5$ km mountain range case. v profiles for<br>$\sigma = .75$ from six-layer and two-layer fine<br>resolution models                                 | 50 |

|     |   |           |    |
|-----|---|-----------|----|
| 16. | $9^\circ \times 1.5$ km mountain range case. v profiles for $\sigma = .25$ and $\sigma = .75$ from two-layer fine resolution model  | - - - - - | 51 |
| 17. | $9^\circ \times 1.5$ km mountain range case. Six-layer coarse resolution model streamlines for $\sigma = .75$   | - - - - - | 52 |
| 18. | $9^\circ \times 1.5$ km mountain range case. v profiles for $\sigma = .91667$ from six-layer fine resolution and six-layer coarse resolution models   | - - - - - | 53 |
| 19. | v profiles from two-layer coarse resolution model for $\sigma = .75$ : $9^\circ \times 1.5$ km mountain range case vs. $9^\circ \times 2.4$ km mountain range case and $9^\circ \times 3.0$ km mountain range | - - - - - | 54 |
| 20. | $3^\circ \times 1.5$ km mountain range case. Six-layer fine resolution model streamlines for $\sigma = .91667$  | - - - - - | 55 |
| 21. | $3^\circ \times 1.5$ km mountain range case. Analytic v profile for $\sigma = 1.0$ vs. six-layer fine resolution model v profile for $\sigma = .91667$  | - - - - - | 56 |
| 22. | $3^\circ \times 1.5$ km mountain range case. Six-layer fine resolution model v profiles for $\sigma = .91667$ , $\sigma = .58333$ , and $\sigma = .25$  | - - - - - | 57 |
| 23. | $3^\circ \times 1.5$ km mountain range case. Analytic v profile for $\sigma = 0.0$ vs. six-layer fine resolution v profile for $\sigma = .083333$   | - - - - - | 58 |
| 24. | $3^\circ \times 1.5$ km mountain range case. Streamlines for $\sigma = .75$ from six-layer fine resolution and two-layer fine resolution models   | - - - - - | 59 |
| 25. | $3^\circ \times 1.5$ km mountain range case. v profiles for $\sigma = .75$ from six-layer fine resolution and two-layer fine resolution models  | - - - - - | 60 |
| 26. | $3^\circ \times 1.5$ km mountain range case. v profiles for $\sigma = .25$ from six-layer fine resolution and two-layer fine resolution models  | - - - - - | 61 |

LIST OF SYMBOLS AND ABBREVIATIONS

|                |   |
|----------------|---|
| a              | Earth's radius  |
| B              | Arbitrary constant in stream function   |
| c <sub>p</sub> | Specific heat for dry air at constant pressure                                |
| F <sub>ε</sub> | Frictional stress (zonal)   |
| F <sub>η</sub> | Frictional stress (meridional)  |
| f              | Coriolis parameter  |
| g              | Gravitational acceleration  |
| H              | Scale height of atmosphere  |
| h              | Height of mountain  |
| L              | Horizontal length scale   |
| L <sub>R</sub> | Rossby radius of deformation  |
| m              | $\frac{1}{a \cos \phi}$   |
| mb             | millibars   |
| N              | Brünt Vaisala frequency   |
| NACA           | National Advisory Committee on Aeronautics                                    |
| n              | $\frac{1}{a}$   |
| p              | pressure  |
| p <sub>s</sub> | surface pressure  |
| p <sub>T</sub> | constant pressure at top of numerical model                                   |
| p <sub>o</sub> | 1000 mb   |
| Q              | Moisture source or sink term  |
| R              | Specific gas constant for dry air   |
| ṡ              | Area-pressure-weighted vertical velocity                                      |
| t              | time  |
| t <sub>p</sub> | Length of period over which topography is introduced into the numerical model |

|                |  |
|----------------|--|
| T              | temperature  |
| u              | zonal component of wind  |
| v              | meridional component of wind   |
| $\alpha$       | Specific volume  |
| $\beta$        | Derivative of Coriolis parameter with respect to the meridional coordinate |
| $\eta$         | Meridional coordinate of the curvilinear coordinate system                 |
| $\theta$       | Potential temperature  |
| $\theta_s$     | Mean state potential temperature   |
| $\kappa$       | $R/c_p$  |
| $\lambda$      | Longitude  |
| $\mu$          | Vertical coordinate in transformed potential vorticity equation            |
| $\xi$          | Zonal coordinate of the curvilinear coordinate system                      |
| $\sigma$       | Dimensionless vertical coordinate  |
| $\dot{\sigma}$ | Measure of vertical velocity   |
| $\Phi$         | Geopotential   |
| $\Phi_s$       | Geopotential of the lower boundary of the numerical model                  |
| $\phi$         | Latitude   |
| $\psi$         | Stream function  |
| $\Omega$       | Angular velocity of the earth  |

#### ACKNOWLEDGEMENT

The authors wish to thank Professor G. J. Haltiner for reviewing the manuscript and making several useful suggestions. Much appreciation is extended to the staff of the W. R. Church Computer Center for computations. J. L. Hayes wishes to give a special loving thanks to his wife, Sharon, and two daughters for their unfailing support over the past year and a half.



## I. INTRODUCTION

For many years, it has been clear that mountain barriers have important effects on cyclones and long waves as well as local effects such as mountain waves. The proper incorporation of topographic features and their effects in numerical models is, therefore, a prerequisite to accurate forecasts.

Most numerical weather prediction models use a form of topography which is linearly smoothed according to grid size. Linear smoothing is a very serious restriction as may be seen in the hypothetical case posed by Charney (1967). An infinitesimally narrow mountain ridge, oriented along a meridian and extending to the top of the atmosphere, would act as an absolute barrier to the flow. Smoothing, however, reduces the mountain height, and therefore its effect, to zero.

An equally significant problem is that the dynamical mechanisms by which mountains influence large scale flow are still not fully understood. Earlier investigations, reviewed by Queney (1973), dealt with linearized flow over topography and were primarily concerned with smaller scale features. Recently, Merkine (1975) considered the interaction of vertically-sheared, inviscid, steady flow with an infinitely long ridge; the formulation was based on approximating the horizontal momentum by the geostrophic momentum. Merkine and Kalnay-Rivas (1976) applied the same model to the three-dimensional flow over an isolated topographic feature.

The main purpose of this study was to investigate the nature of the atmospheric response to mountains of varying widths and heights. The

primitive equation model developed by Monaco and Williams (1975) was used with a cyclic lateral boundary condition to simulate steady westerly flow past a mountain ridge of finite length, oriented perpendicular to the mean flow in the middle latitudes of the northern hemisphere. In addition, the ability of the finite difference model to resolve various features of the flow is considered. A simplified case with features quite similar to those of the model atmosphere was solved analytically in a manner similar to Merkine (1975). This solution was then compared with numerical solutions obtained using various horizontal and vertical resolutions in the model.

## II. DESCRIPTION OF MODEL AND INITIALIZATION PROCEDURES

The two-level general circulation model used in this research has been described by Monaco and Williams (1975). A brief summary of the model together with changes made during this research is presented here.

### A. MODEL DESCRIPTION

The Monaco-Williams model is a modified version of the UCLA general circulation model described in detail by Arakawa and Mintz (1974). The atmosphere is treated as adiabatic and frictionless with no sources or sinks. The equations are written in the vertical  $\sigma$ -coordinate system where:

$$\sigma = \frac{p - p_T}{\pi} \quad (2.1)$$

$$\pi \equiv p_s - p_T$$

where  $p$  is the pressure,  $p_T$  is the constant pressure at the top of the model atmosphere, and  $p_s$  is the surface pressure. The vertical boundaries of the model are the earth's surface and the 200 mb constant pressure level; hence, from (2.1), it follows that:

$$\begin{aligned} \sigma &= 1 & \text{at} & \quad p = p_s \\ \sigma &= 0 & \text{at} & \quad p = p_T = 200 \text{ mb} \end{aligned} \quad (2.2)$$

The boundary condition,  $\dot{\sigma} = \frac{d\sigma}{dt} = 0$ , is applied at the upper and lower boundaries. The atmosphere in between is divided into layers of equal

$\Delta\sigma$ . The structure and the vertical distribution of variables is shown in figure 1 for the two-layer version of the model. The prognostic variables, which are horizontal velocity, temperature, and surface pressure, are governed by the primitive equations:

$$\begin{aligned} \frac{\partial}{\partial t} \left( \frac{\pi}{mn} u \right) + \frac{\partial}{\partial \xi} \left( \frac{\pi u}{n} u \right) + \frac{\partial}{\partial \eta} \left( \frac{\pi v}{m} u \right) + \frac{\partial}{\partial \sigma} \left( \frac{\pi \dot{\sigma}}{mn} u \right) - \left[ \frac{f}{mn} + (v \frac{\partial}{\partial \xi} \frac{1}{n} - u \frac{\partial}{\partial \eta} \frac{1}{m}) \right] \pi v \\ + \frac{\pi}{n} \left[ \frac{\partial \Phi}{\partial \xi} + \sigma \alpha \frac{\partial \pi}{\partial \xi} \right] = \frac{\pi}{mn} F_\xi , \end{aligned} \quad (2.3a)$$

$$\begin{aligned} \frac{\partial}{\partial t} \left( \frac{\pi}{mn} v \right) + \frac{\partial}{\partial \xi} \left( \frac{\pi u}{n} v \right) + \frac{\partial}{\partial \eta} \left( \frac{\pi v}{m} v \right) + \frac{\partial}{\partial \sigma} \left( \frac{\pi \dot{\sigma}}{mn} v \right) + \left[ \frac{f}{mn} + (v \frac{\partial}{\partial \xi} \frac{1}{n} - u \frac{\partial}{\partial \eta} \frac{1}{m}) \right] \pi u \\ + \frac{\pi}{m} \left[ \frac{\partial \Phi}{\partial \eta} + \sigma \alpha \frac{\partial \pi}{\partial \eta} \right] = \frac{\pi}{mn} F_\eta , \end{aligned} \quad (2.3b)$$

$$\begin{aligned} \frac{\partial}{\partial t} \left( \frac{\pi}{mn} c_p T \right) + \frac{\partial}{\partial \xi} \left( \frac{\pi u}{n} c_p T \right) + \frac{\partial}{\partial \eta} \left( \frac{\pi v}{m} c_p T \right) + \left( \frac{p}{p_0} \right)^K \frac{\partial}{\partial \sigma} \left( \frac{\pi \dot{\sigma}}{mn} c_p \theta \right) = \\ \pi \sigma \alpha \left[ \frac{\partial}{\partial t} \left( \frac{\pi}{mn} \right) + \frac{u}{n} \frac{\partial \pi}{\partial \xi} + \frac{v}{m} \frac{\partial \pi}{\partial \eta} \right] + \frac{\pi}{mn} Q , \end{aligned} \quad (2.4)$$

$$\frac{\partial}{\partial t} \left( \frac{\pi}{mn} \right) + \frac{\partial}{\partial \xi} \left( \pi \frac{u}{n} \right) + \frac{\partial}{\partial \eta} \left( \pi \frac{v}{m} \right) + \frac{\partial}{\partial \sigma} \left( \frac{\pi \dot{\sigma}}{mn} \right) = 0 , \quad (2.5)$$

$$p\alpha = RT , \quad (2.6)$$

$$\frac{\partial \Phi}{\partial \sigma} = -\pi\alpha . \quad (2.7)$$

Here,  $\frac{1}{m} = a \cos \phi$ ,  $\frac{1}{n} = a$ ; a complete listing of symbols for the above equations may be found at the beginning of this report. The model's

diagnostic variables include the vertical  $\sigma$ -velocity,  $\dot{\sigma}$ , and geopotential,  $\phi$ . The vertical  $\sigma$ -velocity is given by:

$$\frac{\pi}{mn} \dot{\sigma} = - \int_0^{\sigma} \left[ \frac{\partial}{\partial \xi} \left( \frac{\pi u}{n} \right) + \frac{\partial}{\partial \eta} \left( \frac{\pi v}{m} \right) \right] d\sigma - \sigma \frac{\partial}{\partial t} \left( \frac{\pi}{mn} \right) . \quad (2.8)$$

Geopotentials are determined in a manner which maintains the integral property of the vertically-integrated pressure gradient and conserves total energy. This requires combining the vertical integral of the hydrostatic equation (2.9a) with an alternate form of the hydrostatic equation written in terms of potential temperature (2.9b):

$$\Phi_s = \int_0^1 \Phi d\sigma - \pi \int_0^1 \sigma \alpha d\sigma , \quad (2.9a)$$

$$\frac{\partial \Phi}{\partial p} = - c_p \theta . \quad (2.9b)$$

The horizontal distribution of variables (figure 2) follows Arakawa's "Scheme C" which is designed to simulate accurately the geostrophic adjustment process. A detailed discussion of this scheme and its properties is given by Arakawa and Mintz (1974). In this research, the latitudinal spacing of the  $\pi$  points was fixed at  $4^\circ$ . In the longitudinal direction, two different grid resolutions were considered: coarse ( $\Delta\lambda = 4.5^\circ$ ) and fine ( $\Delta\lambda = 1.5^\circ$ ). Cyclic continuity with wave number 8 was assumed in the  $\xi$ -direction. To avoid the use of an extremely short time step due to the convergence of meridians at the poles, the  $\xi$ -component of the pressure gradient force and the divergence in the  $\xi$ -direction are zonally smoothed as noted by Monaco and Williams (1975). The time integration proceeds in sequence of five time steps: one Matsuno forward/backward step followed by four leapfrog steps. As

noted by Williams (1976), the definitions of  $(\frac{\pi}{mn})$  and  $(\frac{\pi}{mn} \dot{\sigma})$  at u and v points in the finite difference forms of the zonal and meridional momentum equations were changed to the more complex forms described by Arakawa and Mintz (1974).

## B. ANALYTIC INITIALIZATION

Initial conditions were similar to those described by Monaco and Williams (1975). Haurwitz (1940) and Neamtan (1946) obtained the stream function solution to the linearized barotropic vorticity equation. Phillips (1959) used this solution in the forcing function to obtain the geopotential from the non-linear balance equation.

Following these results, an atmosphere in solid rotation (no vertical shear) was simulated by initializing the model with the following equations:

$$\begin{aligned}\psi &= -B a^2 \sin \phi \\ \Phi' &= \frac{1}{2} B a^2 (2\Omega + B) \\ u &= -\frac{1}{a} \frac{\partial \psi}{\partial \phi} = Ba \cos \phi \\ v &= \frac{1}{a \cos \phi} \frac{\partial \psi}{\partial \lambda} = 0\end{aligned}\tag{2.10}$$

where  $\Phi'$  is the geopotential perturbation and  $B$  is a constant; the other terms are defined at the beginning of this report. By setting  $B = \frac{20}{a} \text{ sec}^{-1}$ , a zonal wind distribution which varies as the cosine from the equator (where  $u = 20 \text{ m-sec}^{-1}$ ) to the poles (where  $u = 0 \text{ m-sec}^{-1}$ ) was initially specified. The initial temperature distribution was according to the NACA standard atmosphere as defined in Haltiner and Martin (1957).

### C. INTRODUCTION OF TOPOGRAPHY INTO THE MODEL

An initial problem to be overcome was the adjustment of the model to the topography. Adjustment (or, in this case, steady state) was assumed if all surface pressure tendencies were of the order of 0.25 mb/hour or less and fluctuations in certain arbitrarily selected wind components were of the order of  $0.1 \text{ m-sec}^{-1}/\text{hour}$  or less. A special scheme was used to introduce the topography into the model in order to minimize the time required to reach steady-state. The height of the lower boundary was initially set to zero everywhere. Heights at mountain grid points were then incremented during the integration as a function of time until the desired heights were reached. The equation used at these grid points is:

$$\Phi_s = M \sin^2 \left( \frac{\pi t}{2t_p} \right), \quad t \leq t_p$$

$$M, \quad t \geq t_p \quad (2.11)$$

where  $\Phi_s$  is the height of the mountain at time,  $t$ ;  $M$  is the desired mountain height; and  $t_p$  is the period of time over which the mountains are "built". A typical time series of the surface pressure tendency at a grid point in the vicinity of the mountains is shown in figure 3 for an integration of the two-layer fine resolution model with  $t_p = 16$  hours. Note that the largest tendency ( $\sim 15$  mb/hour) is observed at mid-period; this corresponds to the maximum rate of change of the mountain height defined by (2.11). With one exception, it appears that steady-state has been achieved at 16 hours. One attempt to reduce  $t_p$  to 12 hours resulted in lengthening the adjustment time. In addition, it was necessary to increase  $t_p$  to 36 hours for the coarse resolution model.

### III. ANALYTIC INVESTIGATION

Merkine (1975) considered a steady, Boussinesq flow with no vertical shear past a large mountain ridge in a rotating, stratified atmosphere, bounded above by a horizontal rigid lid. He was able to analytically solve the potential vorticity equation with appropriate boundary conditions; he was also able to derive and solve an analytic equation for the  $v$  component of the wind. He performed this analysis on an  $f$ -plane with infinite boundaries in the upstream and downstream directions; in addition, he assumed the flow to be balanced in the vertical and cross-topography directions (similar to Hoskins and Bretherton, 1972; and Hoskins, 1974). If these same assumptions are made together with a lateral boundary condition of cyclic continuity, an analytic solution can be derived for a simplified case which is quite similar to the numerical integrations which are presented in this report. The two-dimensional potential vorticity equation (independent of  $y$ ) for inviscid, adiabatic, Boussinesq flow on an  $f$ -plane may be written:

$$\frac{d}{dt} \left[ \left( \frac{\partial v}{\partial x} + f \right) \frac{\partial \theta}{\partial z} - \frac{\partial v}{\partial z} \frac{\partial \theta}{\partial x} \right] = 0 \quad (3.1)$$

Consider the solution:

$$\left( \frac{\partial v}{\partial x} + f \right) \frac{\partial \theta}{\partial z} - \frac{\partial v}{\partial z} \frac{\partial \theta}{\partial x} = \text{constant} \quad (3.2)$$

In order to determine the constant, equation (3.2) is evaluated away from the mountains where there is no horizontal or vertical shear to give:

$$f \frac{\partial \theta_s}{\partial z} = \text{constant} \quad (3.3)$$

where  $\theta_s(z)$  represents the mean state potential temperature at level  $z$ .

Using the geostrophic relation,  $v = \frac{1}{f} \frac{\partial \Phi}{\partial x}$ , and the hydrostatic relation,  $\theta = \theta_s(z) + \frac{\theta_o}{g} \frac{\partial \Phi}{\partial z}$ , equation (3.2) may be written:

$$\frac{1}{f} \frac{\partial^2 \Phi}{\partial x^2} N^2 + \frac{1}{f^2} \frac{\partial^2 \Phi}{\partial x^2} \frac{\partial^2 \Phi}{\partial z^2} + \frac{\partial^2 \Phi}{\partial z^2} - \frac{1}{f^2} (\frac{\partial^2 \Phi}{\partial x \partial z})^2 = 0 \quad (3.4)$$

where  $N^2 = \frac{g}{\theta_o} \frac{\partial \theta_s}{\partial z}$ .

In order to non-dimensionalize this equation, the following scale factors (also used by Merkine (1975)) are introduced:

$$\begin{aligned} \Phi &= N^2 H^2 \Phi' \\ z &= Hz' \\ x &= \frac{NH}{f} x' \end{aligned} \quad (3.5)$$

The non-dimensional form of (3.4) may then be written:

$$\frac{\partial^2 \Phi'}{\partial x'^2} + \frac{\partial^2 \Phi'}{\partial x'^2} \frac{\partial^2 \Phi'}{\partial z'^2} + \frac{\partial^2 \Phi'}{\partial z'^2} - (\frac{\partial^2 \Phi'}{\partial x' \partial z'})^2 = 0, \quad (3.6)$$

or, dropping the prime notation:

$$\Phi_{xx}(1 + \Phi_{zz}) + \Phi_{zz} - \Phi_{xz}^2 = 0, \quad (3.7)$$

where the subscripts  $x, z$  indicate differentiation with respect to a particular variable - e.g.,  $\Phi_x = \frac{\partial \Phi}{\partial x}$ . This is similar to the equation derived by Merkine (1975); he further showed that this equation can be transformed into Laplace's equation under a non-linear transformation. First, equation (3.7) is differentiated with respect to  $z$ , and  $\phi$  is replaced by  $\psi$  through the following equation:

$$\psi = \Phi_z + z - 1. \quad (3.8)$$

Here,  $\psi$  is the non-dimensional stream function for flow in the  $x-z$  plane. In a steady-state, the non-dimensional potential temperature,  $\Phi_z + z$ , is constant along a streamline. The new equation in terms of  $\psi$  can be written:

$$\psi_{xx} \psi_z^2 + (\psi_x^2 + 1) \psi_{zz} - 2\psi_x \psi_z \psi_{xz} = 0 . \quad (3.9)$$

Now a transformation of variables is made so that  $\psi$  is the new vertical coordinate. With this transformation equation (3.9) becomes:

$$z_{xx} + z_{\psi\psi} = 0 , \quad (3.10)$$

where  $z$  is now a dependent variable which represents the height of the isentropic surfaces. It is convenient to define the new variable

$$\mu = z - \psi + 1 . \quad (3.11)$$

In terms of  $\xi$  the basic equation and boundary conditions are:

$$\mu_{xx} + \mu_{\psi\psi} = 0$$

$$\mu = 0 \text{ at } \psi = 0 , \quad (3.12)$$

$$\mu = \frac{h}{H} f(S^{1/2}x)$$

where  $f(S^{1/2}x)$  is a function specifying the height of the lower boundary. Since the numerical model invokes cyclic continuity as the lateral boundary condition, let

$$f(S^{1/2}x) = \cos(S^{1/2}x) \quad (3.13)$$

where  $S^{1/2} = \frac{2\pi L_R}{L} = \frac{2\pi NH}{fL}$ ; in dimensional form (3.13) becomes

$\cos\left(\frac{2\pi x^*}{L}\right)$ , where the (\*) denotes dimensional form. Setting  $\mu = \cos(s^{1/2}x)G(\psi)$ , it may be shown that (3.12) reduces to:

$$\begin{aligned} G''(\psi) - SG(\psi) &= 0 \\ G(0) &= 0 \\ G(-1) &= \frac{h}{H} \end{aligned}, \quad (3.14)$$

which has as a solution:

$$G(\psi) = A \sinh(s^{1/2}\psi) + B \cosh(s^{1/2}\psi). \quad (3.15a)$$

Equation (3.15a) is evaluated at the boundaries to determine the constants A and B with the following result:  $A = -\frac{h}{H \sinh s^{1/2}}$ ,  $B = 0$ ; hence the solution to (3.12) may be written:

$$\mu = -\frac{h}{H} \frac{\sinh(s^{1/2}\psi)}{\sinh(s^{1/2})} \cos(s^{1/2}x). \quad (3.15b)$$

Making use of the transformation rules and the equations of motion, it can be shown that:

$$\begin{aligned} \frac{\partial v}{\partial \psi} &= \frac{\partial \mu}{\partial x} \\ \frac{\partial v}{\partial x} &= -\frac{\partial \mu}{\partial \psi} \end{aligned}, \quad (3.16)$$

and that the v component is determined by the system:

$$\begin{aligned} v_{xx} + v_{\psi\psi} &= 0 \\ v_\psi &= 0 \quad \text{at } \psi = 0 \\ v_\psi &= -\frac{h}{H} s^{1/2} f'(s^{1/2}x) \quad \text{at } \psi = -1 \end{aligned}, \quad (3.17)$$

By letting  $f'(s^{1/2}x) = -\sin(s^{1/2}x)$  and  $v = F(\psi) \sin(s^{1/2}x)$ , this system may be solved in the same manner as above; hence,

$$v(x, \psi) = -\frac{h \cosh(s^{1/2}\psi)}{H \sinh s^{1/2}} \sin(s^{1/2}x) . \quad (3.18)$$

Note that

$$v_{top} = v(x, 0) = -\frac{h}{H \sinh s^{1/2}} \sin(s^{1/2}x) , \quad (3.19a)$$

$$v_{bottom} = v(x, -1) = -\frac{h}{H \tanh s^{1/2}} \sin(s^{1/2}x) , \quad (3.19b)$$

are the solutions at the upper and lower boundaries. The fully dimensional forms of  $v$  at the lower and upper boundaries may be written:

$$v_b^* = -\frac{Nh}{\tanh(\frac{2\pi Nh}{fL})} \sin\left(\frac{2\pi x^*}{L}\right) , \quad (3.20)$$

$$v_t^* = -\frac{Nh}{\sinh(\frac{2\pi Nh}{fL})} \sin\left(\frac{2\pi x^*}{L}\right) . \quad (3.21)$$

The asterisks are used here as a reminder that  $x$  and  $v$  are in their dimensional forms;  $v_b^*$ ,  $v_t^*$  represent values at the lower and upper boundaries respectively. Considering the lower boundary,  $v_b^*$  may be written as the sum of an infinite series:

$$v_b^* = -\sum_{n=1}^{\infty} \frac{Nh}{\tanh(\frac{2\pi Nh}{fL/n})} \sin\left(\frac{2\pi x^*}{L/n}\right) . \quad (3.22)$$

In a finite difference model, this summation must be truncated after wave number  $n_{max} = \frac{L}{2\Delta x}$  (the maximum wave number resolvable by the grid).

The height of the mountain ridge,  $h_n$ , is specified in the following manner. In the dimensional form,  $z_b^*$ , the height of the lower boundary may be written:

$$\begin{aligned} z_b^* &= h \cos\left(\frac{2\pi x^*}{L}\right) \\ &= h f(x^*) , \end{aligned} \quad (3.23)$$

where  $f(x^*)$  is a functional representation of the shape of the topography varying from 0 at the base of the mountain to 1 at its top.

In this investigation, only mountains symmetric (in the east-west direction) about the ridge line were considered (see figure 4). The exact functional form of the mountain may be written:

$$\begin{aligned} f\left(\frac{nx^*}{L}\right) &= 1 - \frac{n|x|}{L\pi\varepsilon} & - \frac{\varepsilon\pi L}{n} \leq x & \leq \frac{\varepsilon\pi L}{n} \\ &= 0 . & \frac{\varepsilon\pi L}{n} \leq |x| & \leq \frac{\pi L}{n} \end{aligned} \quad (3.24)$$

$f\left(\frac{nx^*}{L}\right)$  may also be represented by the following Fourier-cosine series:

$$f\left(\frac{nx^*}{L}\right) = A_0 + \sum_{n=1}^{\infty} A_n \cos\left(\frac{2\pi nx^*}{L}\right) , \quad (3.25)$$

where:  $A = \frac{\varepsilon}{2}$ ,

$$A_n = \frac{2(1-\cos(n\pi\varepsilon))}{n^2\pi^2\varepsilon} . \quad (3.25a)$$

The height of the mountain ridge (at  $x^* = 0$ ) may then be written:

$$h = h_0 + \sum_{n=1}^{\infty} h_n , \quad (3.26)$$

where:  $h_0 = h A_0$  (3.26a)

$$h_n = h A_n \quad (3.26b)$$

$h_0$  does not contribute to the v component; therefore, (3.26b) is used in equation (3.22) to derive  $v_b^*$ .

In order to analytically approximate the conditions present in the numerical model, the series approximations for  $v_t^*$  and  $v_b^*$  were truncated after wave number  $n = \frac{L}{2\Delta x}$ . For example, a 30-point grid can resolve only 15 wave numbers; therefore, the series approximations are truncated after 15 terms. The  $v_b^*$  analytic profile for a  $9^\circ \times 1.5$  km (width x height) mountain computed on a 30-point grid spanning one cycle of wave number 8 is shown in figure 5 where the origin of the graph is placed at the mountain top. Since a 30-point grid on wave number 8 results in  $1.5^\circ$  resolution, the mountain is carried (by non-zero  $z_b^*$ ) at five grid points. Superimposed is the same analytic case computed with twice the resolution; this results in the mountain being represented by 11 grid points. Note that the two profiles at the lower boundary are nearly coincident.

In figure 6 is shown the  $v_b^*$  analytic profiles for a  $3^\circ \times 1.5$  km mountain computed using a 30-point grid versus the same case using a 60-point grid. In the former case, only one grid point represents the mountain, while three points were used in the latter case. Qualitatively, the two profiles exhibit the same general flow characteristics; however, the fluctuations observed in the profile of the 30 grid point case differ significantly from the smooth profile of the 60 grid point case. When the mountain width was reduced to  $1.5^\circ$  on the 60-point grid (thereby allowing only one grid point to represent the mountain), similar fluctuations were observed. These results seem to indicate that one grid point is an inadequate representation of a mountain with respect to the quantitative aspects of the flow at the lower boundary.

In figure 7, the  $v_t^*$  analytic profiles for a  $3^\circ \times 1.5$  km mountain computed on a 30-point grid versus a 60-point grid are shown. The

similarity between the two profiles indicates that the poor resolution has little effect at the upper boundary. As noted above, a grid with  $1.5^\circ$  resolution appears to be sufficient to accurately specify the flow response to a  $9^\circ$  wide mountain at both the upper and lower boundaries. Therefore, in order to examine the characteristics of the analytic response, consider figure 8 in which the analytic profiles of  $v_t^*$  and  $v_b^*$  are shown for a  $9^\circ \times 1.5$  km mountain computed on a grid with  $1.5^\circ$  resolution. Both profiles are antisymmetric about the mountain indicating ridging centered at the mountain top. A downstream trough, commonly associated with flow over mountains, is located at the eastern boundary. However, in this case, the feature is purely the result of the assumption of cyclic continuity. Had we assumed the lateral boundaries to be infinite, we would have observed downstream a permanent deflection to the south (as noted by Merkine (1975)) because of the assumption of a constant Coriolis parameter. Merkine (1975) also noted that a variable Coriolis force would generate a trough in the downstream region (results from the numerical model support this observation). The lower boundary response, as expected, is greater in magnitude than the upper boundary response. Note that the lower boundary maxima, however, are located closer to the ridge. This would seem to indicate that the smaller scale response is damped more rapidly above the lower boundary. At the ridge itself, both  $v_b^*$  and  $v_t^*$  are zero. It may be seen from (3.20) and (3.21) that varying the mountain height affects the amplitude of the response only. This can be seen from figure 9 in which the  $v_b^*$  profile is shown for a  $9^\circ \times 1.5$  km mountain vs. a  $9^\circ \times 3.0$  km mountain. Increasing the height of the mountain by a factor of two causes a uniform increase (by a factor of two) in the magnitude of the response at both the upper and lower boundaries. This is not true in the interior where non-linear distortions occur.

#### IV. NUMERICAL MODEL RESULTS

A number of integrations were performed using various forms of the model. In each of the experiments, a mountain range of uniform height oriented north-south was centered in the grid. The model was initialized, as earlier described, and integrated forward in time until a steady-state was achieved. In the following discussion again, fine resolution refers to  $1.5^\circ$  longitudinal grid spacing and coarse resolution refers to  $4.5^\circ$  grid spacing.

##### A. BROAD MOUNTAIN RANGE CASE

A mid-latitude mountain range,  $9^\circ \times 1.5$  km (width  $\times$  height), extending from  $34^\circ\text{N}$  to  $66^\circ\text{N}$  was the first case considered. Results from the various integrations are as follows:

###### 1. Six Layer Fine Resolution Model Results

The wind field from level six ( $\sigma = .91667$ ) is shown in figure 10. Significant features include ridging over the mountains and weak troughing downstream. Upstream, the flow is deflected northward by the mountains; downstream, the deflection is southward, becoming weakly northward east of the trough. At a distance from the mountains, both upstream and downstream, little deflection is apparent. Deflection of the flow is also observed one grid point ( $\sim 445$  km) to the north and south of the mountains; this distance is of the order of the Rossby radius of deformation. In figure 11 is shown the wind field at level one ( $\sigma = .08333$ ). In general, the effect of the mountains on flow at this level appears to be minimal. Consider the v profile for level six ( $\sigma = .91667$ )

at  $44^{\circ}\text{N}$  shown in figure 12. This latitude was chosen because it crosses the mountain near the center and, more importantly, because it was representative of the response at the other latitudes which cross the mountains. Superimposed on the  $v$ -profile is the analytic solution,  $v_b^*$ , at  $\sigma = 1.0$  for the similar analytic case. There is significant similarity between the two curves. Both profiles indicate ridging at the mountain top with the only apparent upwind difference being one of magnitude (the model showing a greater northward deflection). Downstream, as in the analytic case, the southward maximum is in the same position, relative to the mountain top, as the northward maximum; however, its magnitude is about twice that of the northward maximum. Also, downstream, the model profile indicates the trough position to be about  $75^{\circ}$  (longitude) east of the mountains; in contrast, the analytic solution shows the trough at the channel's eastern boundary. This difference is to be expected because the Boussinesq approximation and the f-plane and rigid lid assumptions (present in the analytic case) are not made in the numerical model. In figure 13, the  $v$  profiles for levels two, four and six at  $44^{\circ}\text{N}$  are shown. Noting the positions of the northward and southward maxima relative to height, a systematic westward tilt in the vertical is observed; this tilt is not observed in the analytic solution. It is felt that this tilt could be the result of the  $\beta$ -effect and other effects not included in the analytic solution. As noted in the analytic case, the response should damp with height--this is especially apparent in the magnitude of the southward maximum. In figure 14 is shown the analytic solution at  $\sigma = 0$  versus the model profiles for  $\sigma = .08333$  and  $\sigma = .25$ . Note that in both model profiles the magnitude of the response is similar to that of the analytic case, but the horizontal scale is

smaller. In addition, the systematic westward tilt with height is observed in the two model profiles.

## 2. Two Layer Fine Resolution Model Results

The same case was computed using the two layer model to examine the effect of vertical resolution on the numerical simulation of the flow. The  $\sigma = .75$  velocity field was compared with its counterpart from the six layer model and only minor differences (in the vicinity of the mountains) were observed. In figure 15, the v-profiles for  $\sigma = .75$  at  $44^\circ\text{N}$  are shown for these two models. There is little difference between the two curves, both showing a ridge centered one grid point west of the mountains and both showing weak troughing in the same general area downstream. Some differences exist in the vicinity of the mountains, but, in general, the two layer model's response appears to be quite similar to that of the six layer model. In figure 16, the v-profiles at  $\sigma = .75$  and  $\sigma = .25$  from the two layer model are superimposed. As in the case of the six layer model, a westward tilt is again observed.

## 3. Coarse Resolution Model Results

In order to investigate the effect of horizontal grid resolution, the above integrations were repeated using the six-layer and two-layer coarse resolution models. The velocity fields at  $\sigma = .25$  and  $\sigma = .75$  produced by these two models were quite similar. In figure 17 is shown the six-layer model field at  $\sigma = .75$ . In general, it shows a deflection of the flow similar to the six-layer fine resolution model, but differences were noted particularly in the vicinity of the mountains. In figure 18 are shown the v-profiles for the six-layer fine resolution model versus the six-layer coarse resolution model. Note that the magnitudes are about the same but that the scale of the response is less in the fine resolution model. This would appear to emphasize the importance of

horizontal grid resolution in the simulation of finer scale features of the flow over topography.

Consider figure 19 in which the lower level ( $\sigma = .75$ ) v-profiles for the two-layer coarse resolution model are shown for three different mountain height cases (1.5, 2.4, and 3.0 km). The shapes of these three profiles are quite similar with magnitudes increasing with increasing mountain height. Clearly, the response is directly proportional to mountain height as it is in the analytic case at the boundaries. In addition, although the response at the mountain top is non-zero, it is approximately independent of mountain height. Hence, at least some of the gross aspects of the analytic solution are apparent in the coarse resolution simulations.

#### B. NARROW MOUNTAIN RANGE CASE

Next, a narrower mountain range ( $3^\circ$  wide) extending from  $34^\circ\text{N}$  to  $66^\circ\text{N}$  was considered; mountain height was again set at 1.5 km. Since the distance between grid points in the  $\xi$ -direction is  $1.5^\circ$  in the fine resolution model, this allows only one grid point at each latitude to represent the mountains.

##### 1. Six Layer Fine Resolution Model Results

The wind field from level six ( $\sigma = .91667$ ) is shown in figure 20. As in the wider mountain case, there is ridging over the mountains and troughing downstream. However, the magnitude of the deflection in the vicinity of the mountains appears to be much greater in this case. Note that one grid point ( $1.5^\circ$  longitude) west of the mountains, the flow is almost directly from the south the whole length of the mountain range. Significant deflection of the flow is observed one grid point (~445 km) north and south of the mountains as was true in the wide

mountain case. The effect of the mountains on the upper level flow at  $\sigma = 0.08333$  appeared to be minimal (as in the wide mountain case). In figure 21 is shown the v-profile for level six ( $\sigma = 0.91667$ ) at  $44^\circ\text{N}$  superimposed on the analytic solution at  $\sigma = 1.0$  for the same case. The strong northward deflection observed in figure 20 is seen here at grid point 14 as a strong northward maximum exceeding, in magnitude, the analytic solution by a factor of four. While the downstream southward maximum is not coincident with its analytic counterpart, it has the same magnitude as the northward maximum. This symmetric behavior is predicted by the analytic solution and it differs from the result in the wide mountain case where the magnitude of the southward maximum was about twice that of the northward maximum.

The position of the downstream trough is closer (by  $3^\circ$  longitude) to the mountains in this case. Note the similarity between the fluctuations observed in the analytic solution and those appearing in the upstream v-profile. It would appear that these oscillations are a result of allowing only one grid point to represent the mountains interacting with a mean flow from the west. These oscillations are not present in the model's downstream profile. In figure 12 are shown the v-profiles for levels two, four and six. Noting the position of the southward maximum with respect to height, there again appears to be a systematic westward tilt with height; however, it is not as well defined here as in the wider mountain case (figure 15). In figure 23 is shown the analytic solution at  $\sigma = .08333$ . As in the wide mountain case, the amplitudes of the two responses are similar, but the horizontal scale of the model response is much smaller.

## 2. Two Layer Fine Resolution Model Results

An integration for the same case was performed using this version of the model. Comparing the resulting wind field at  $\sigma = .75$  with the six layer model results, significant differences were observed in the vicinity of the mountains (see figure 24). In the six-layer model field, a well-defined, narrow trough broadening toward the south is observed immediately east of the mountains; however, there is no trough in this area in the wind field of the two layer model. Differences were noted in the magnitudes of the wind velocity downstream. Further upstream and downstream, the two models give similar results at this level. A comparison of the fields at  $\sigma = .25$  showed little difference between the two models. In figure 25 are superimposed the v profiles from both models for  $\sigma = .75$  at  $44^\circ\text{N}$ . As can be seen, little differences exist away from the mountains; however, immediately upstream, the oscillations in the six-layer model profile appear to be of greater amplitude, and, downstream, the six-layer model profile shows the presence of a strong trough which is absent in the two-layer model profile. In figure 26, the v-profiles from both models at  $\sigma = .25$  (also at  $44^\circ\text{N}$ ) are shown; the two are similar to the extent of having a principal trough and ridge, but sizable phase differences are seen. These results indicate that the vertical resolution is important in this case.

During the latter stages of this study, a relatively minor coding error was discovered in the computer program; this error had been present throughout the period of this research. As described by Monaco and Williams (1975), a pressure-area-weighted form of the horizontal wind components  $(\frac{\pi u}{mn}, \frac{\pi v}{mn})$  is forecast by the model;  $u$  and  $v$  are computed after each time step by dividing out  $\frac{\pi}{mn}$ . The error resulted in a slight

overestimation of this term in that section of the coding responsible for removing this weighting from the v component after each leapfrog time step. A test case was recomputed using the corrected version of the two-layer coarse resolution model. Almost no change was observed in the wind fields for the  $\sigma = .25$  and  $\sigma = .75$  levels. Although slight changes in the v-profiles were observed, the overall pattern remained the same. It was, therefore, concluded that the error in coding did not significantly affect the nature of the response depicted in these results.

## V. CONCLUSIONS

From the results of the numerical simulations, it is evident that, in general, the mountains interact with the atmospheric flow in such a way as to induce ridging over the mountains and troughing on the downstream side at lower levels. With the exception of the troughing the numerical solution appeared, in general, to agree with the analytic result from the Boussinesq model. The presence of the downstream trough was due to the fact that the numerical model has a variable Coriolis parameter and a non-rigid upper boundary; in contrast, the analytic model considered Boussinesq flow on an f-plane bounded above by a rigid lid.

Several other similarities were observed between the analytic response and the numerical response. As in the analytic case, smaller scale features appeared to damp rapidly with height. Varying the mountain height was, in general, observed to affect the amplitude of the numerical response in the same manner as in the analytic case. Reduction of the width of the mountains reduced the horizontal scale of the numerical response, but in contrast to the analytic solution, it also increased the magnitudes of the northward and southward maxima. It was initially felt that the strong northward maximum along the western side of the  $3^\circ \times 1.5$  km mountains might be related to air flowing around rather than over the mountains. A detailed examination, however, seemed to indicate that this was not the case.

The numerical solution, in every case, displayed a systematic westward tilt with height which was not observed in the analytic solution.

The precise reason for this tilt was not determined; however, it appears to be the result of the  $\beta$ -effect, compressibility and non-rigid upper boundary in the numerical model.

The effect of vertical resolution appeared to be minimal in the case of the broader mountains; but significant effects were observed when the mountain width was reduced. With respect to horizontal resolution, the coarse resolution model appeared to be able to reproduce some of the larger scale features observed in fine resolution solutions; however, differences were noted between the two models with respect to finer scale features of the flow.

Early in this research, an unsuccessful attempt was made to simulate conditions in which air flows around rather than over the mountains. From these results, and those of Merkine (1975), it appears necessary to further reduce the horizontal scale of the mountains. These results also indicate that finer horizontal and vertical resolution would be necessary to accurately simulate the atmospheric response to this narrower mountain range. With the high price paid in computing time for increased resolution, this appears to be a definite argument for the use of a nested grid in treating atmospheric response to mountains.

No problems were encountered in treating unsmoothed topography in the numerical model. In addition, the scheme used to introduce the mountains into the model behaved quite well. Additional attention should be given to the possibility of reducing the period of time necessary to incorporate the mountains. If this can be done, a similar scheme might be used to introduce smaller scale topographical features into operational numerical models.

Finally, this investigation considered a mean flow with no shear in the vertical. Future research should be directed at investigating the response of a vertically-sheared flow to mountains. Another area to be examined is the effect of condensation and the release of latent heat into the air flow.

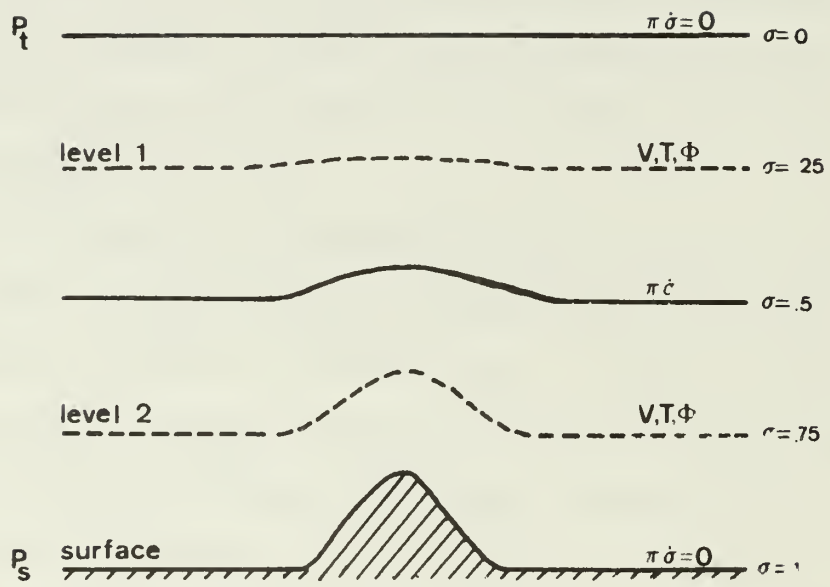


Figure 1. The sigma ( $\sigma$ ) coordinate system as used in the two-layer version of the model. Also shown is the vertical distribution of the variables.

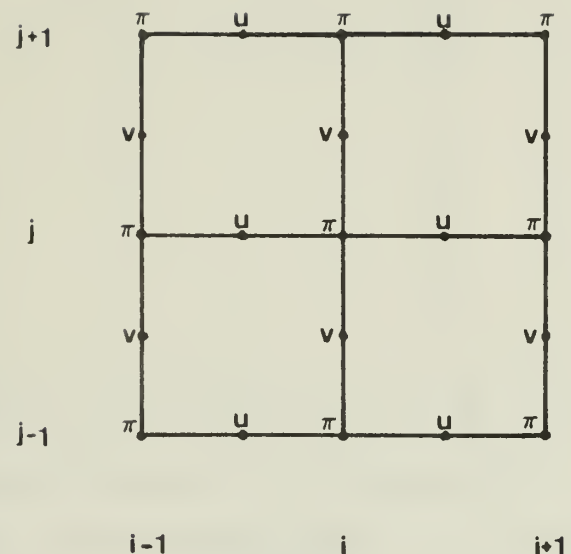


Figure 2. Horizontal distribution of variables.  $\dot{\sigma}$ , T,  $\Phi$  are also carried at  $\pi$  points.

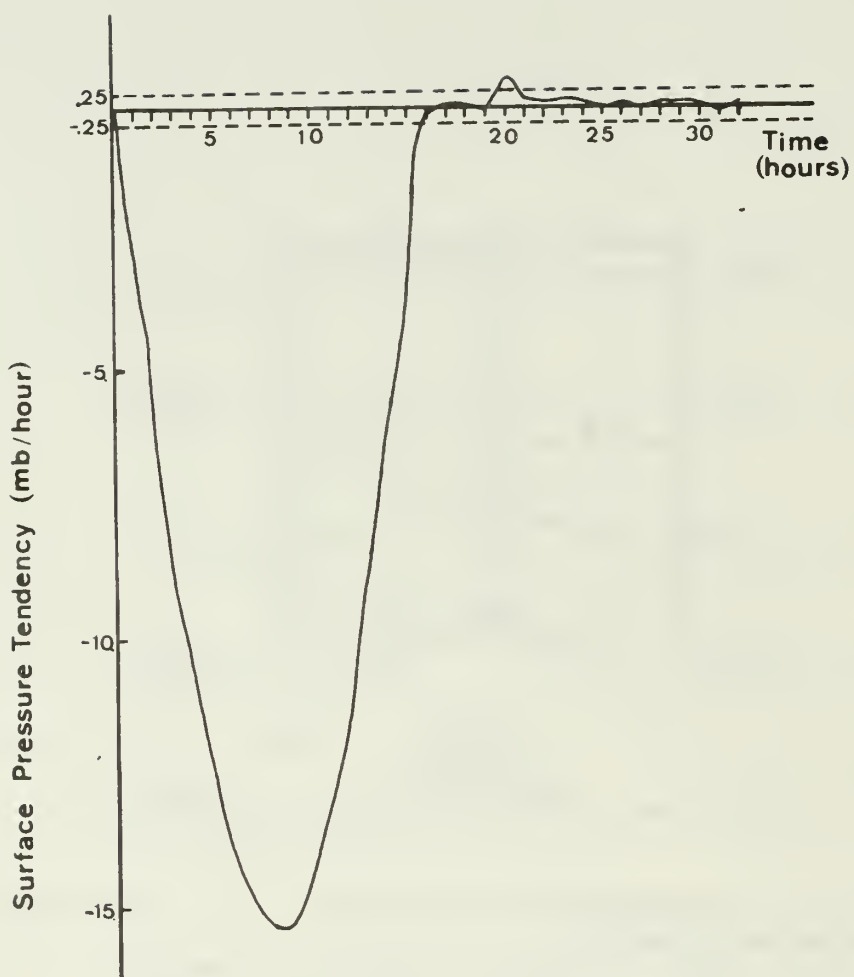


Figure 3. Time variation of the surface pressure tendency from a grid point in the vicinity of the mountains.

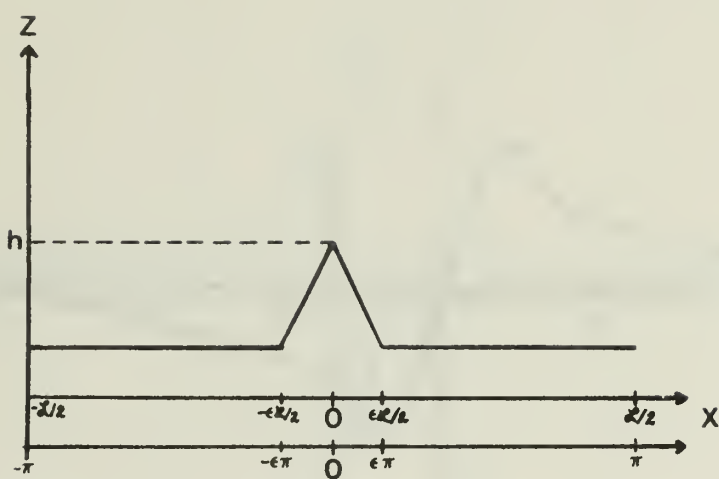


Figure 4. Cross section of the topography.

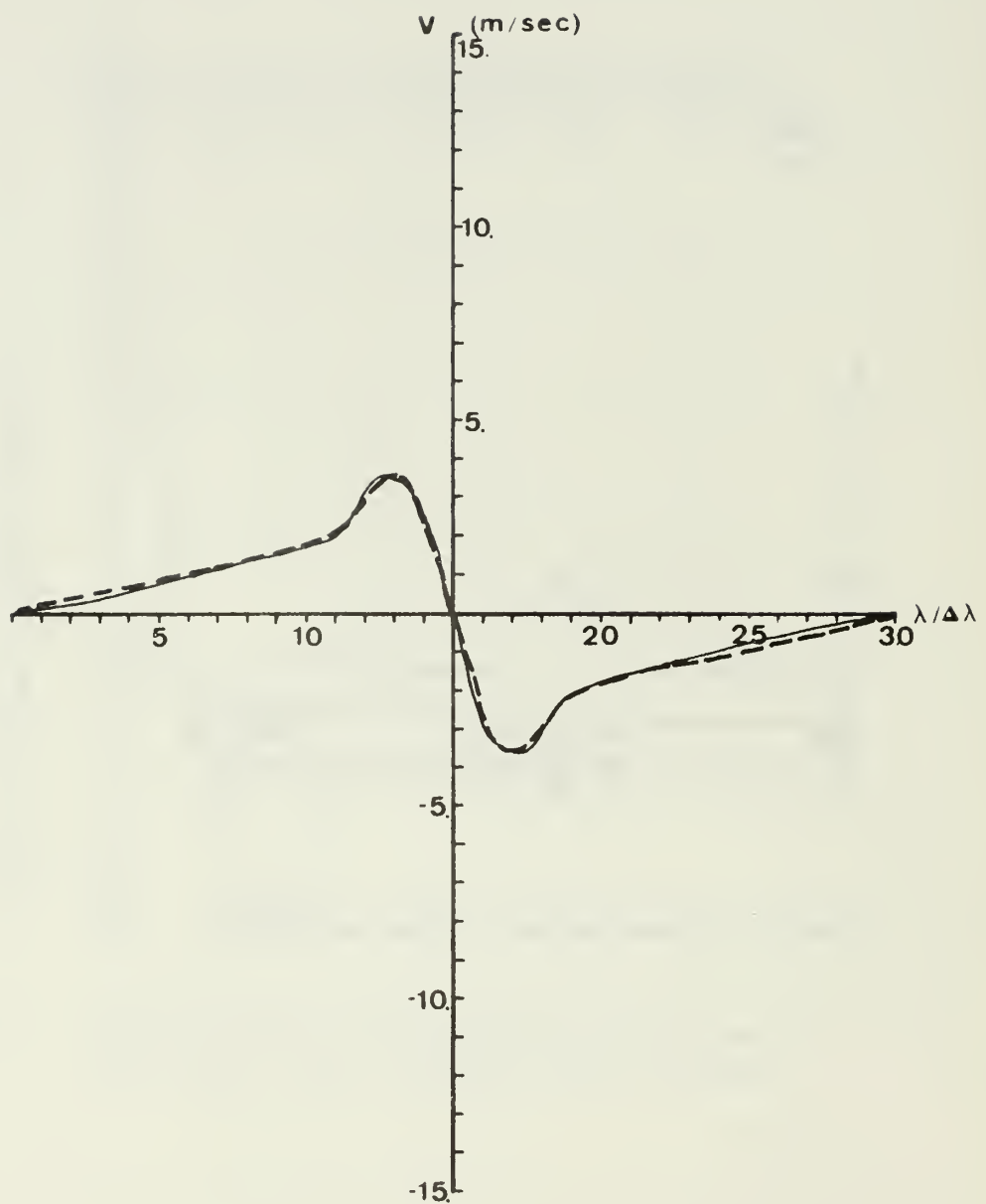


Figure 5.  $9^\circ \times 1.5$  km mountain case. Analytic  $v$  profiles for  $\sigma = 1.0$  at  $44^\circ\text{N}$  computed on a 30 point grid (dashed curve) vs. a 60 point grid (solid curve). Vertical axis is centered at the mountain top.

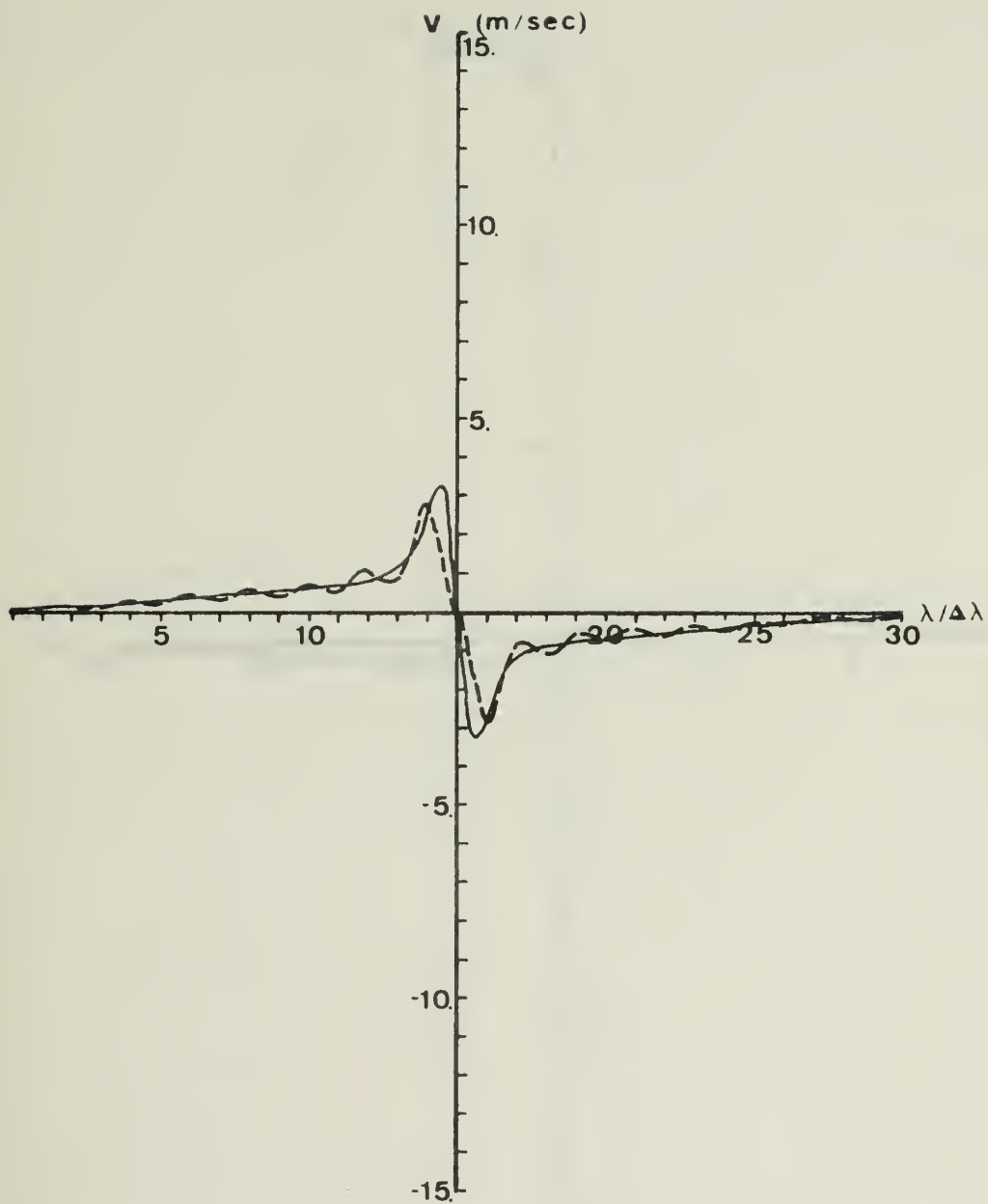


Figure 6.  $3^\circ \times 1.5$  km mountain case. Analytic  $v$  profiles for  $\sigma = 1.0$  at  $44^\circ\text{N}$  computed on a 30 point grid (dashed curve) vs. a 60 point grid (solid curve).

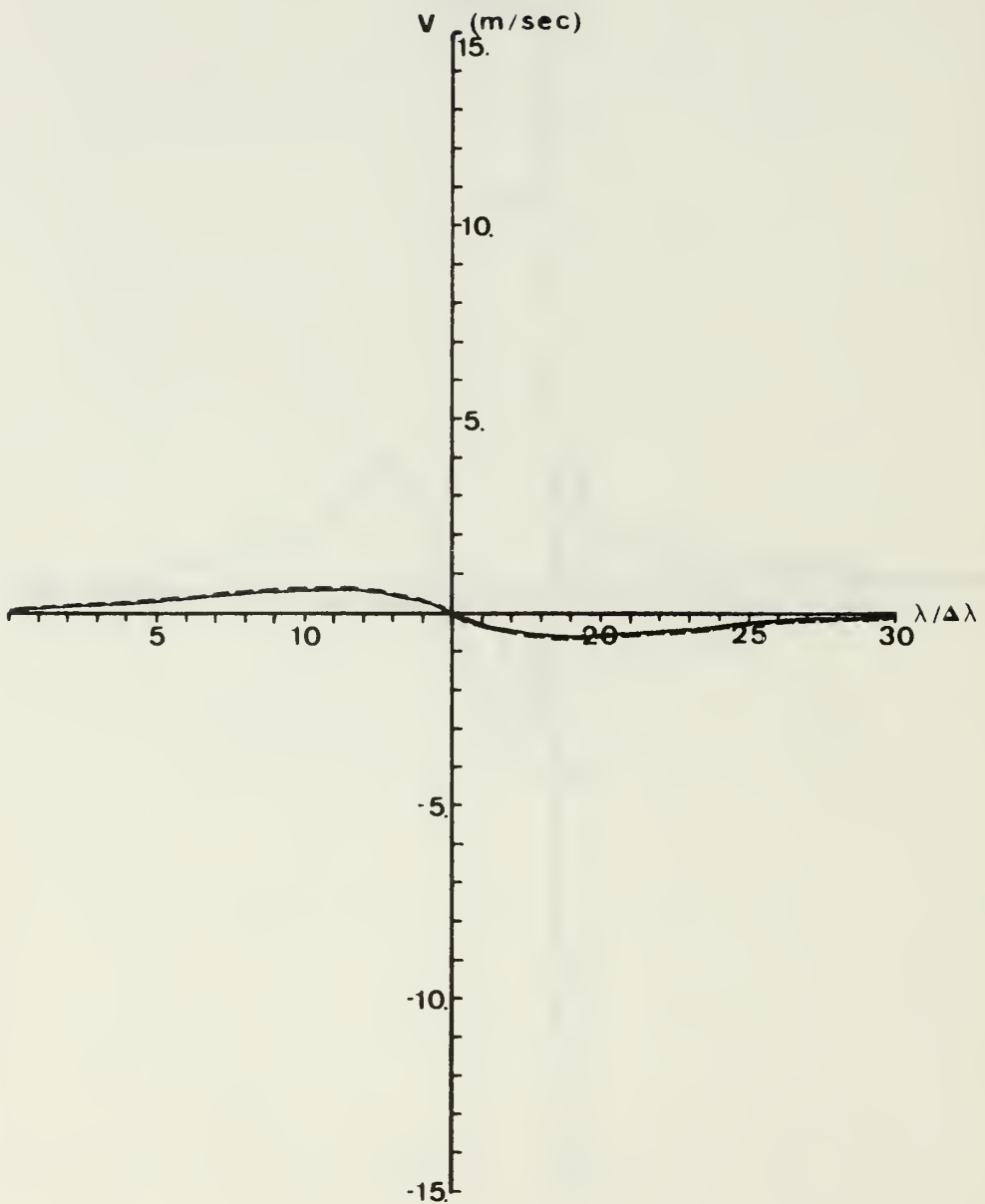


Figure 7.  $3^\circ \times 1.5$  km mountain case. Analytic  $v$  profiles for  $\sigma = 0.0$  at  $44^\circ\text{N}$  computed on a 30 point grid (dashed curve) vs. a 60 point grid (solid curve).

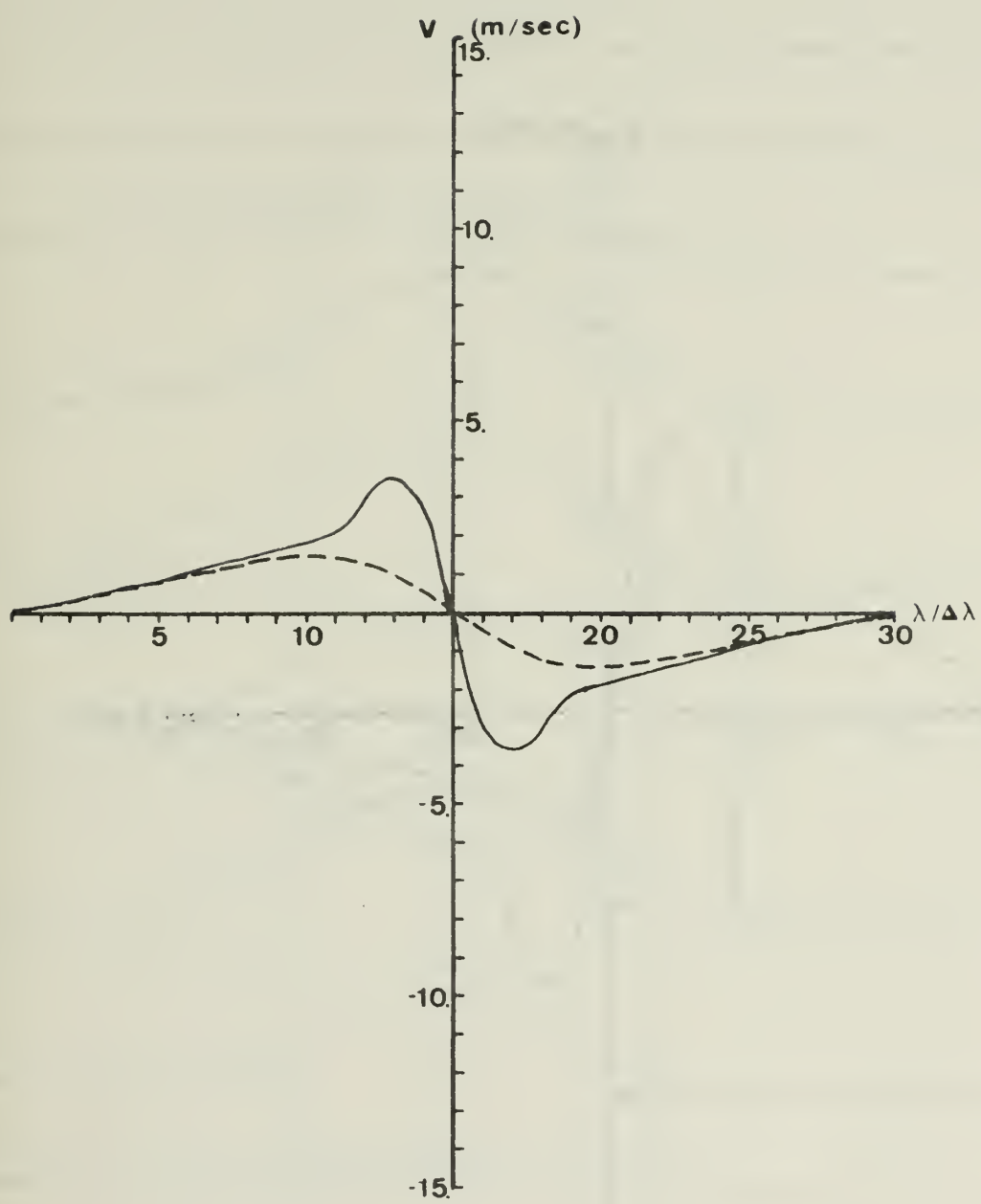


Figure 8.  $9^\circ \times 1.5$  km mountain case. Analytic  $v$  profiles for  $\sigma = 1.0$  (solid curve) and  $\sigma = 0.0$  (dashed curve) computed on a 30 point grid.

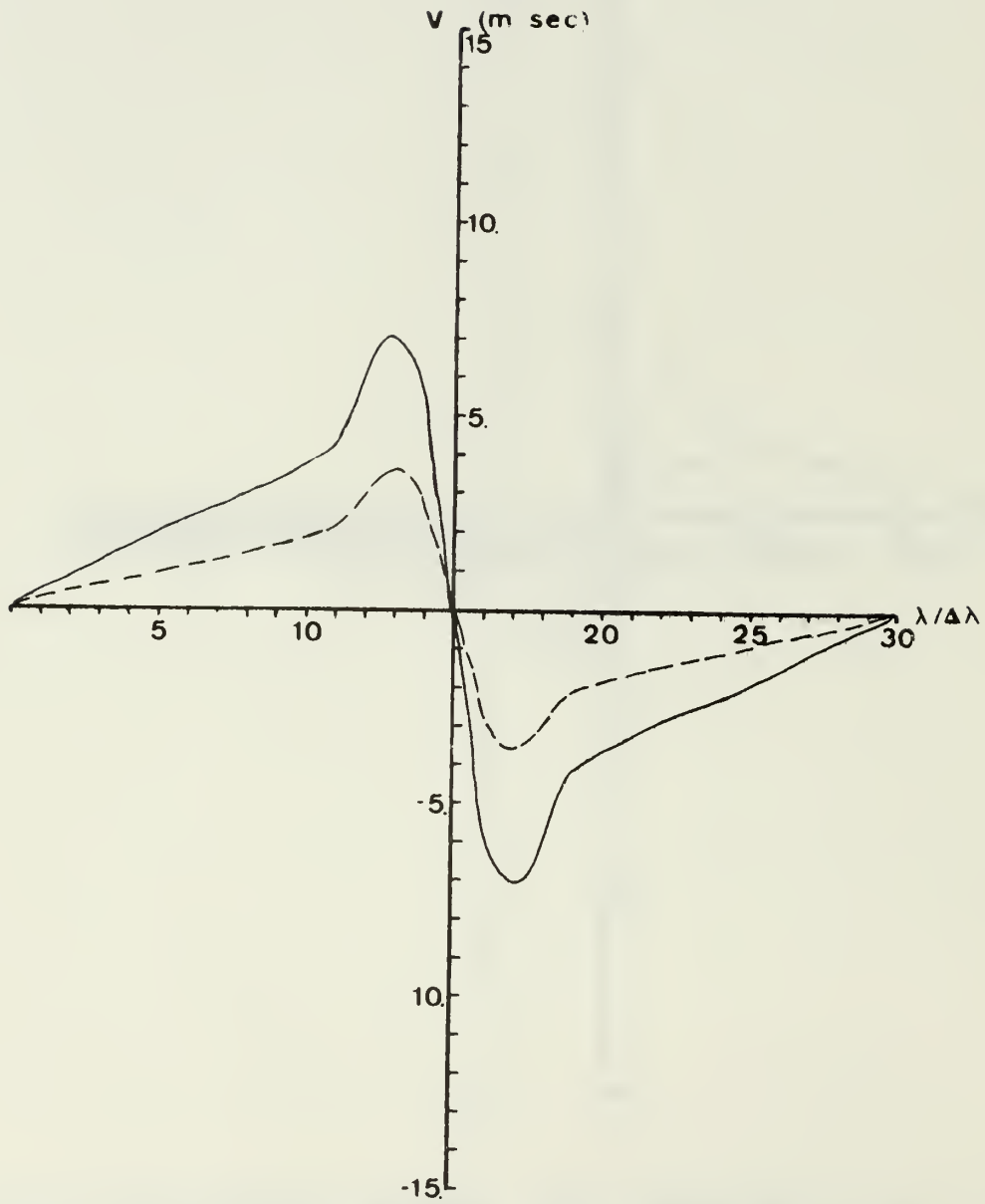


Figure 9. Analytic  $v$  profiles for  $\sigma = 1.0$  at  $44^\circ\text{N}$  computed on a 30 point grid for a  $9^\circ \times 1.5 \text{ km}$  mountain (dashed curve) vs. a  $9^\circ \times 3.0 \text{ km}$  mountain (solid curve).

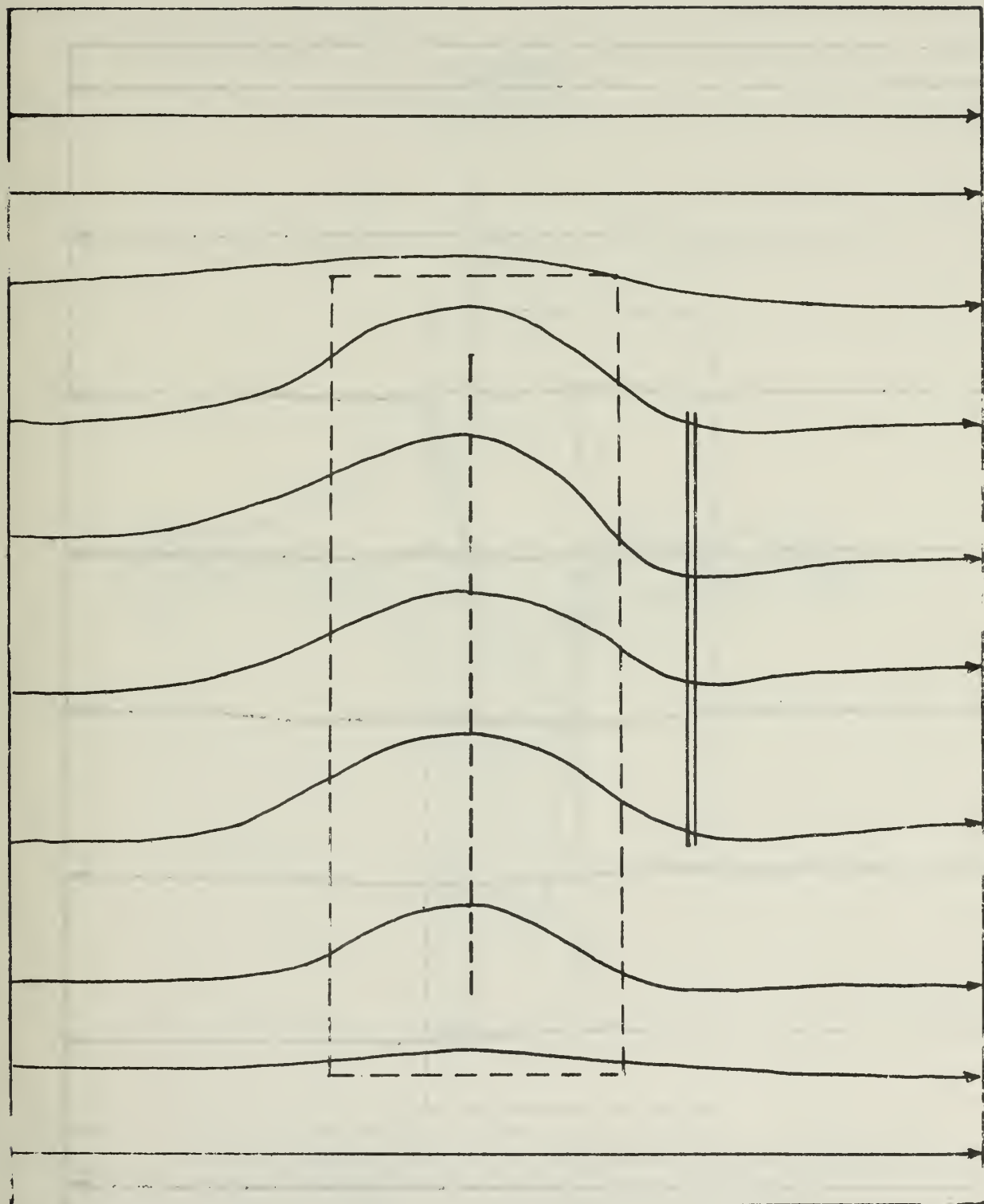


Figure 10.  $9^\circ \times 1.5$  km mountain range case. Six-layer fine resolution model streamlines for  $\sigma = .91667$ . Dashed lines depict outline of mountain range and mountain ridge line.

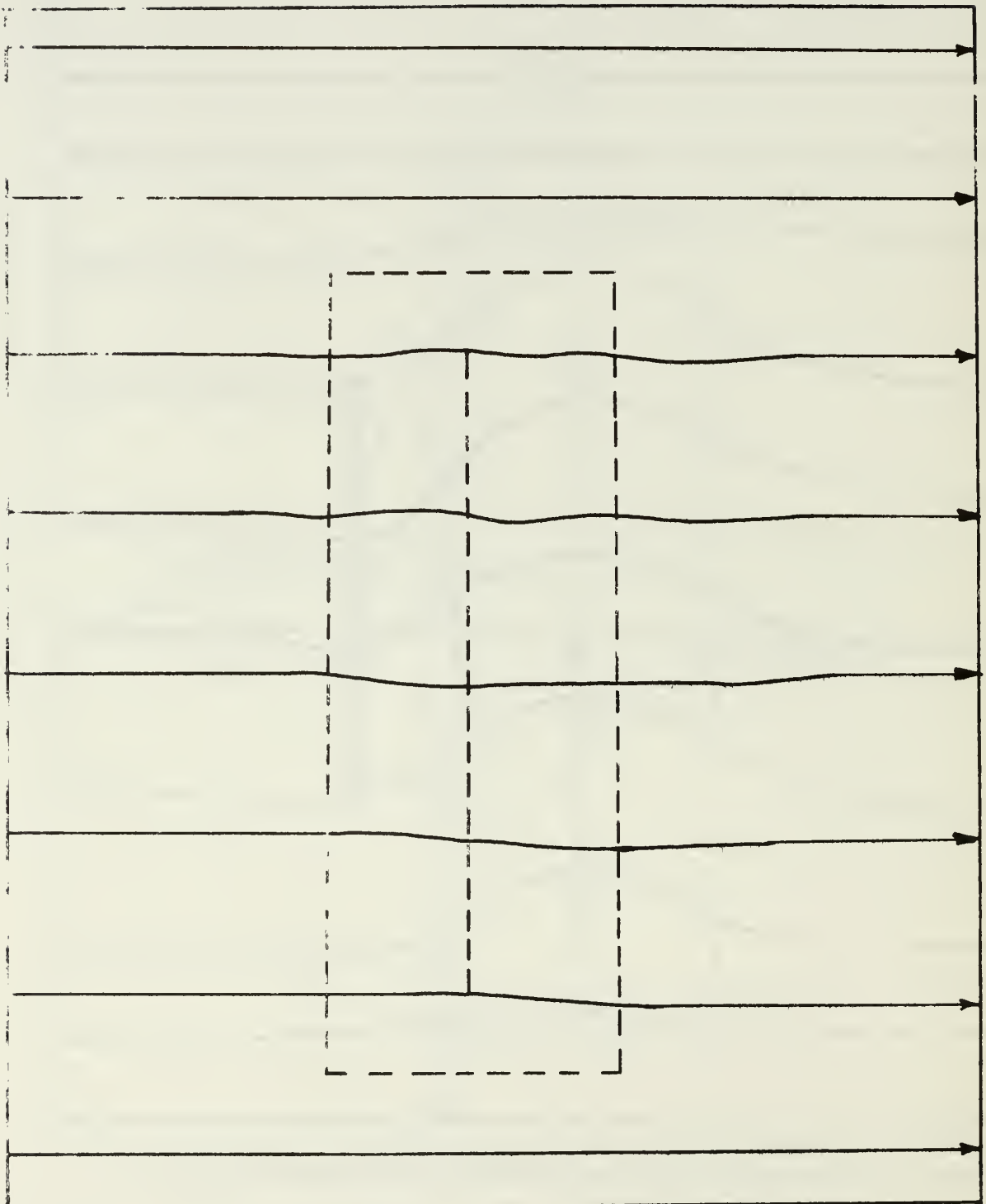


Figure 11.  $9^\circ \times 1.5$  km mountain range case. Six-layer fine resolution model streamlines for  $\sigma = .08333$ .

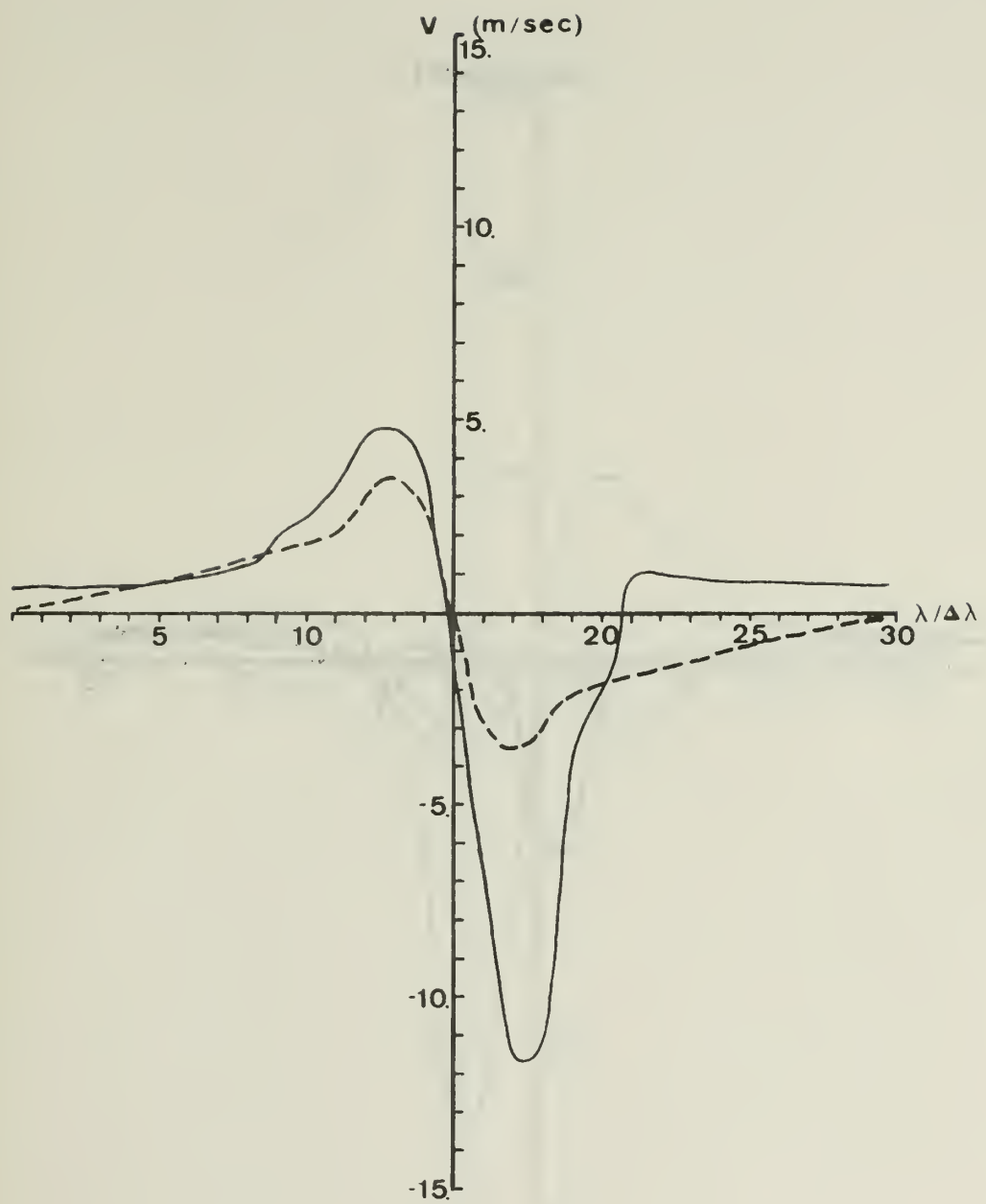


Figure 12.  $9^\circ \times 1.5$  km mountain range case. Analytic  $v$  profile for  $\sigma = 1.0$  (dashed curve) vs. six-layer fine resolution model  $v$  profile for  $\sigma = .91667$  (both at  $44^\circ\text{N}$ ).

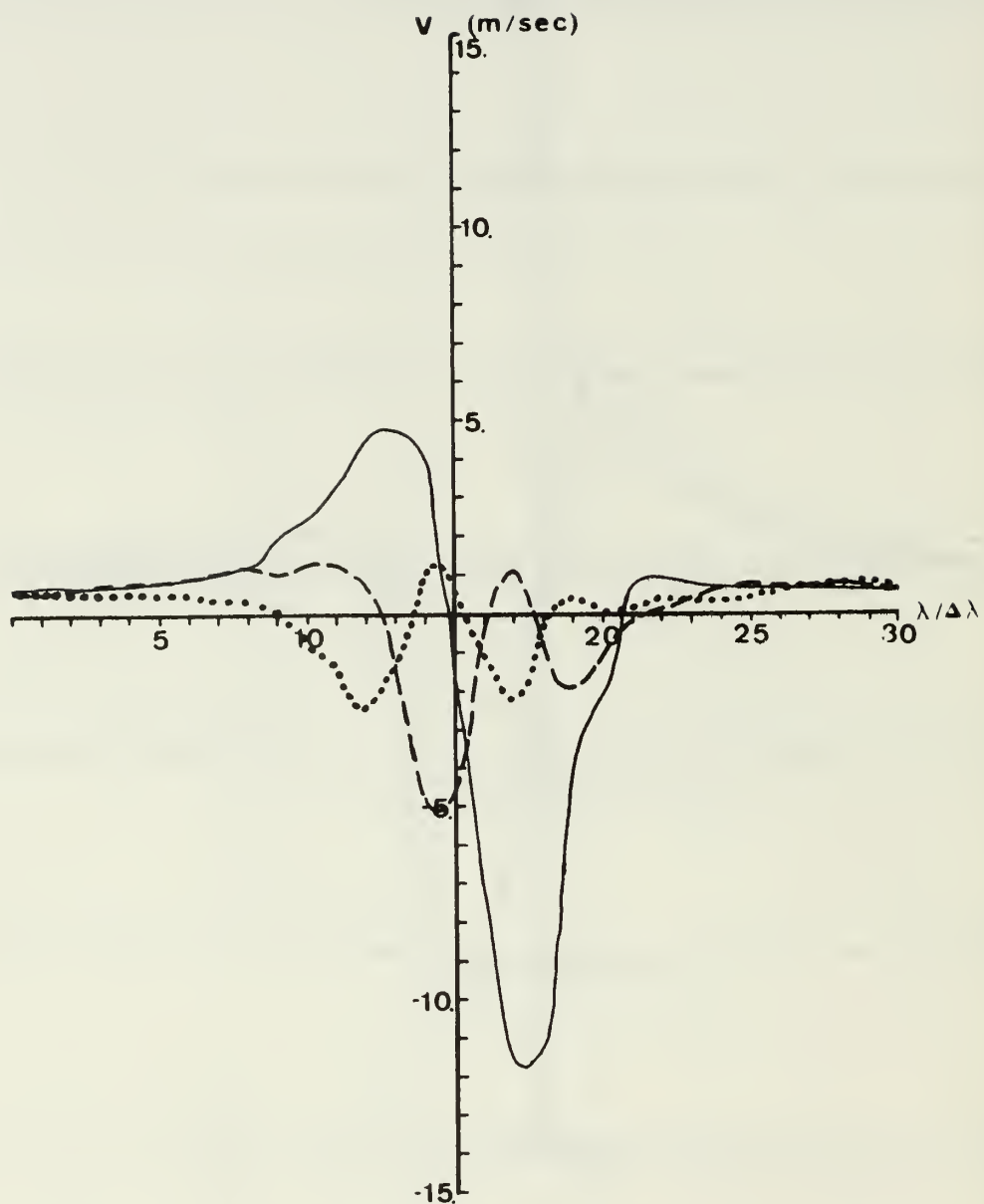


Figure 13.  $9^\circ \times 1.5$  km mountain range case. Six-layer fine-resolution model  $v$  profiles for  $\sigma = .25$  (dotted curve),  $\sigma = .58333$  (dashed curve),  $\sigma = .91667$  (solid curve), all at  $44^\circ\text{N}$ .

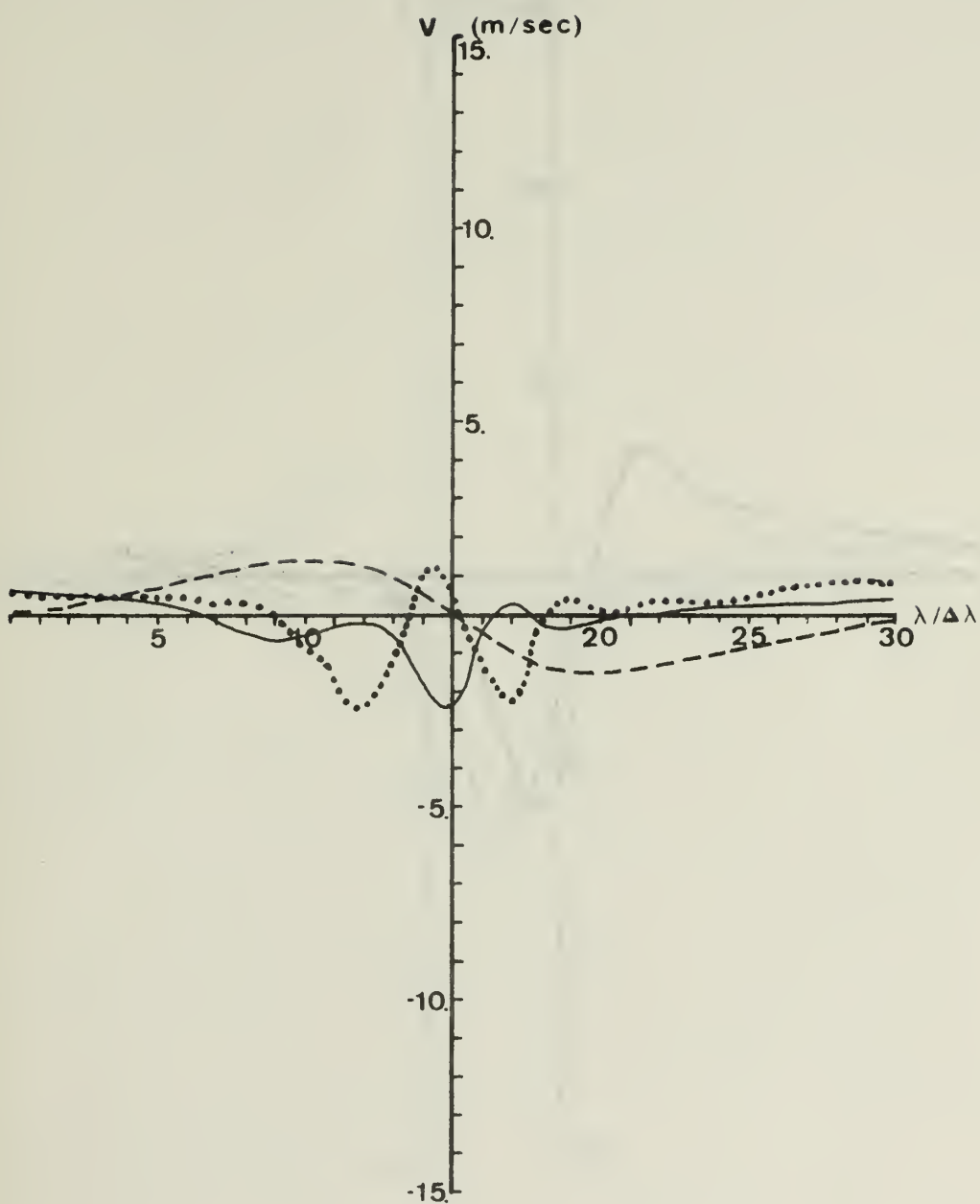


Figure 14.  $9^\circ \times 1.5$  km mountain range case. Analytic  $v$  profile for  $\sigma = 0.0$  (dashed curve) vs. six-layer fine-resolution model  $v$  profiles for  $\sigma = .083333$  (solid curve) and  $\sigma = .25$  (dotted curve), all at  $44^\circ\text{N}$ .

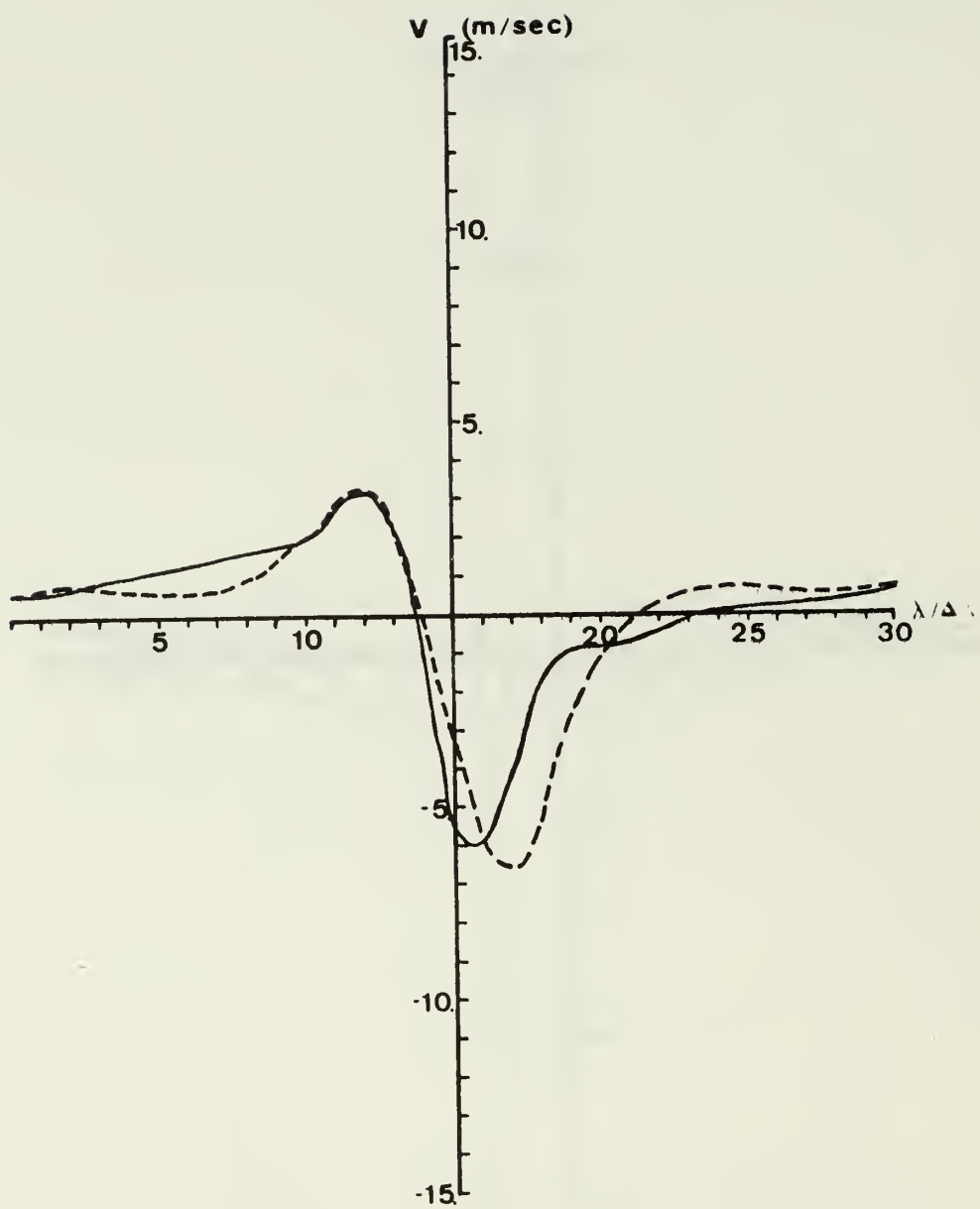


Figure 15.  $9^\circ \times 1.5$  km mountain range case.  $v$  profiles for  $\sigma = .75$  at  $44^\circ\text{N}$  from six-layer fine resolution model (solid curve) and two-layer fine resolution model (dashed curve).

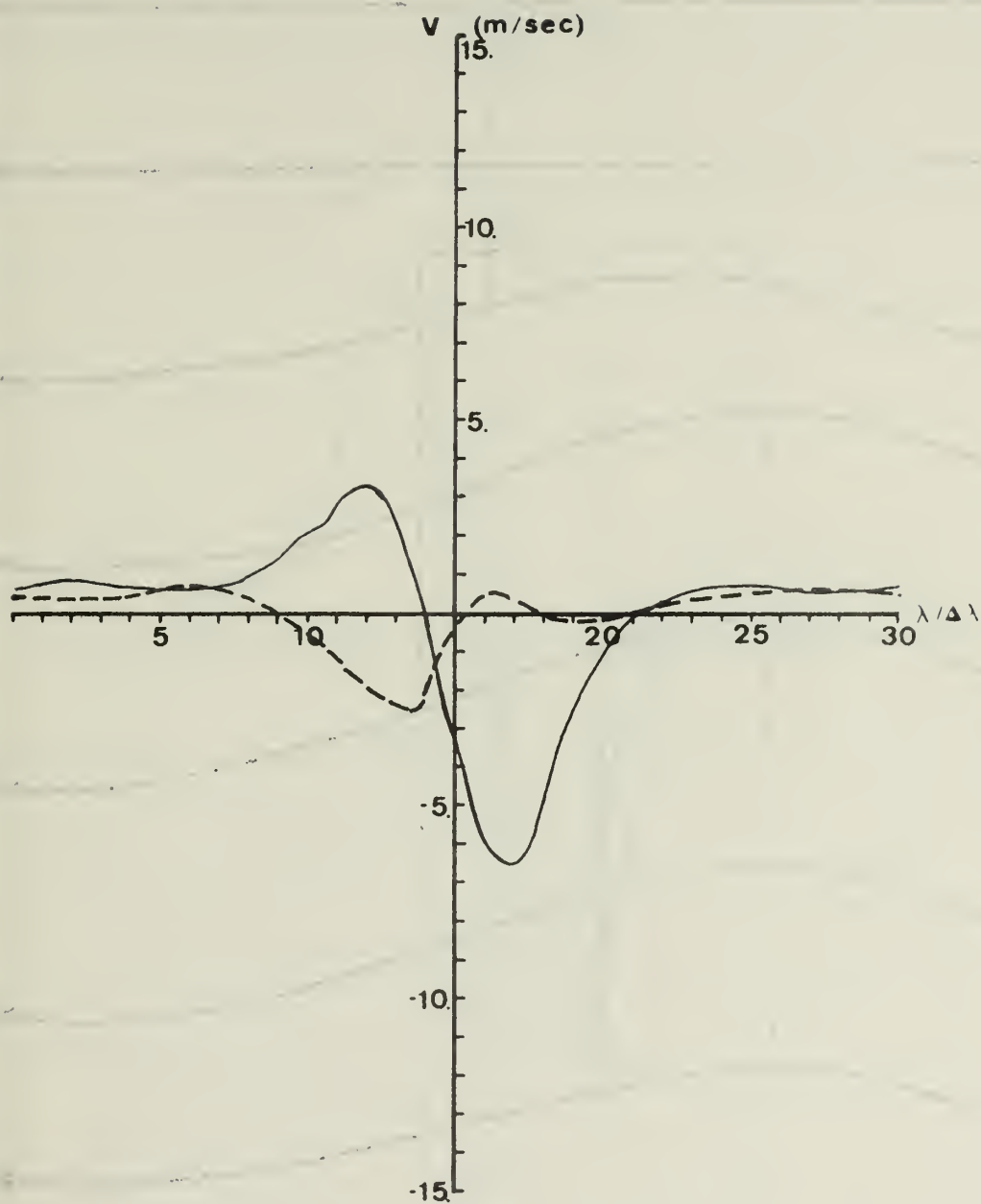


Figure 16.  $9^\circ \times 1.5$  km mountain range case.  $v$  profiles for  $\sigma = .25$  (dashed curve) and  $\sigma = .75$  (solid curve) at  $44^\circ\text{N}$  from two-layer fine resolution model.

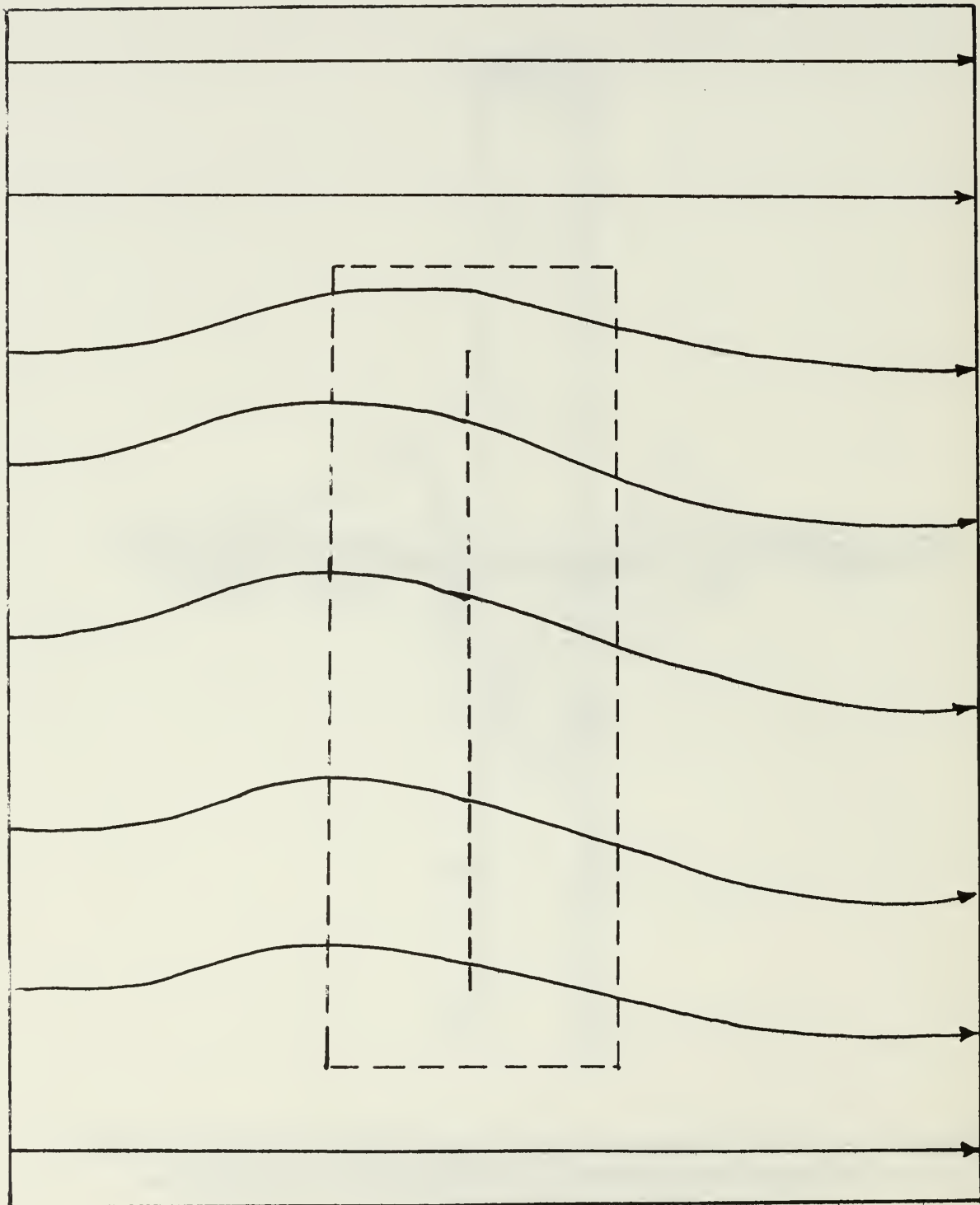


Figure 17.  $9^\circ \times 1.5$  km mountain range case. Six-layer coarse resolution model streamlines for  $\sigma = .75$ .

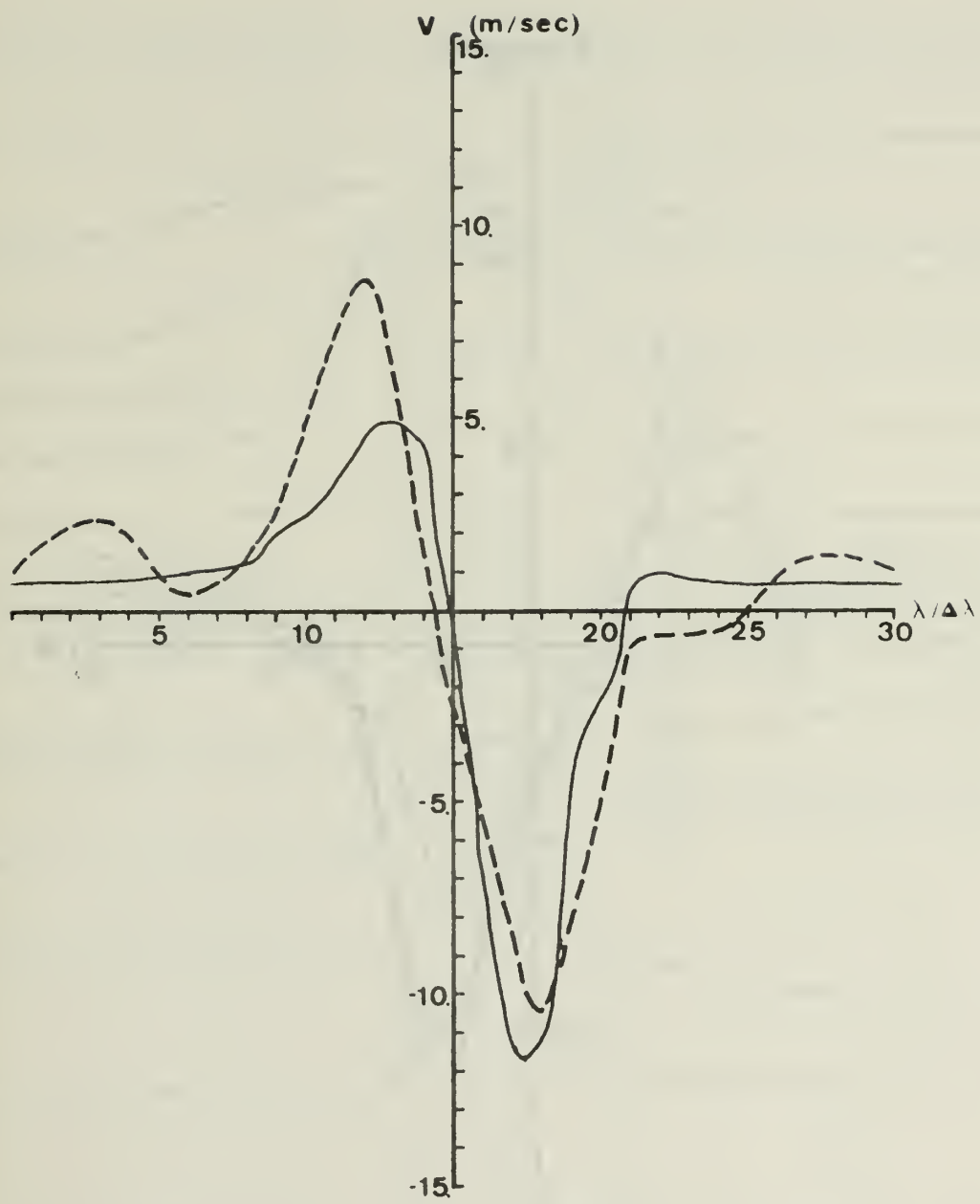


Figure 18.  $9^\circ \times 1.5$  km mountain range case.  $v$  profiles for  $\sigma = .91667$  at  $44^\circ\text{N}$  from six-layer fine resolution model (solid curve) and six-layer coarse resolution model (dashed curve).

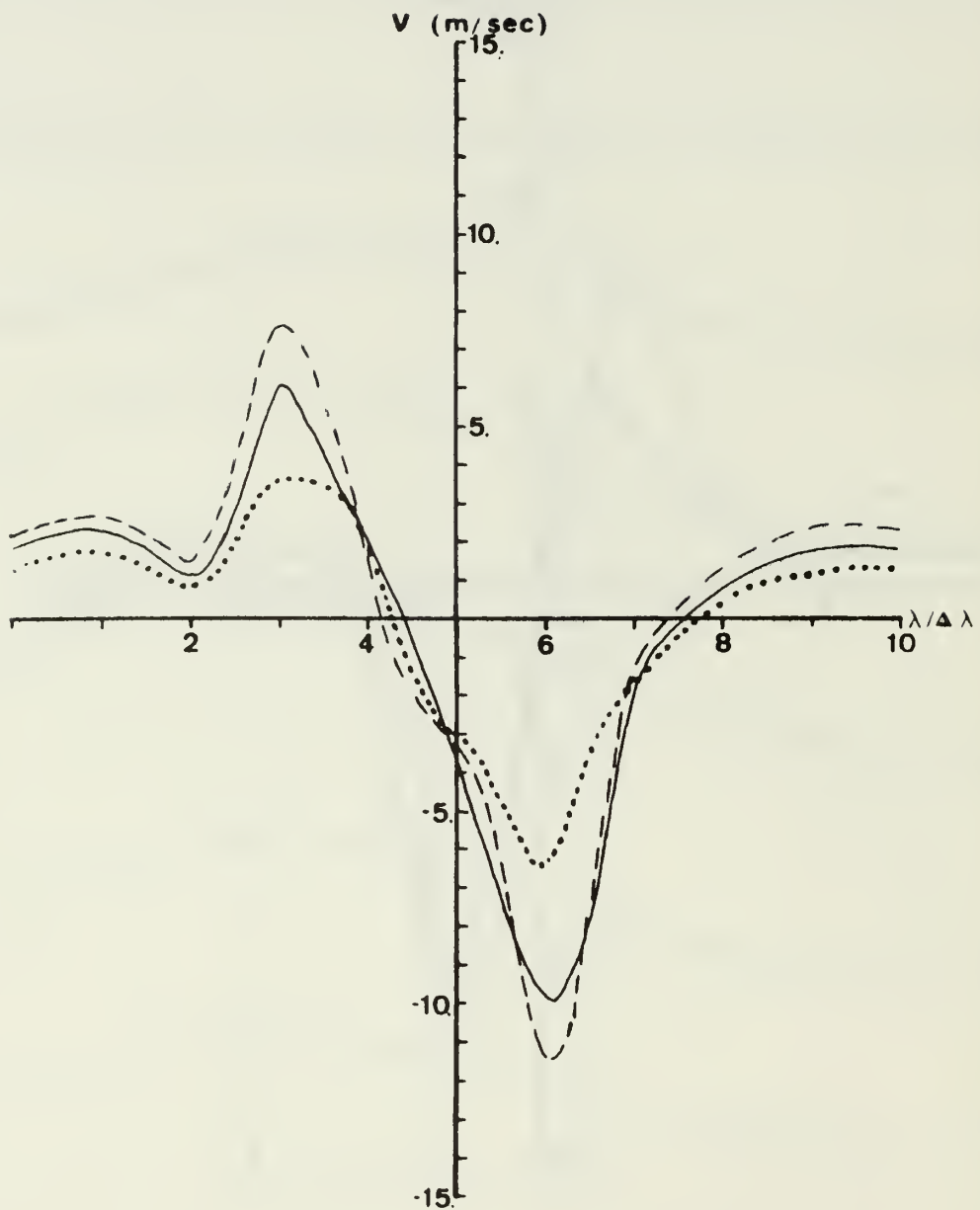


Figure 19.  $v$  profiles from two-layer coarse resolution model for  $\sigma = .75$  at  $44^\circ\text{N}$  for the following cases:  $9^\circ \times 1.5 \text{ km}$  mountain range (dotted curve),  $9^\circ \times 2.4 \text{ km}$  mountain range (solid curve),  $9^\circ \times 3.0 \text{ km}$  mountain range (dashed curve).

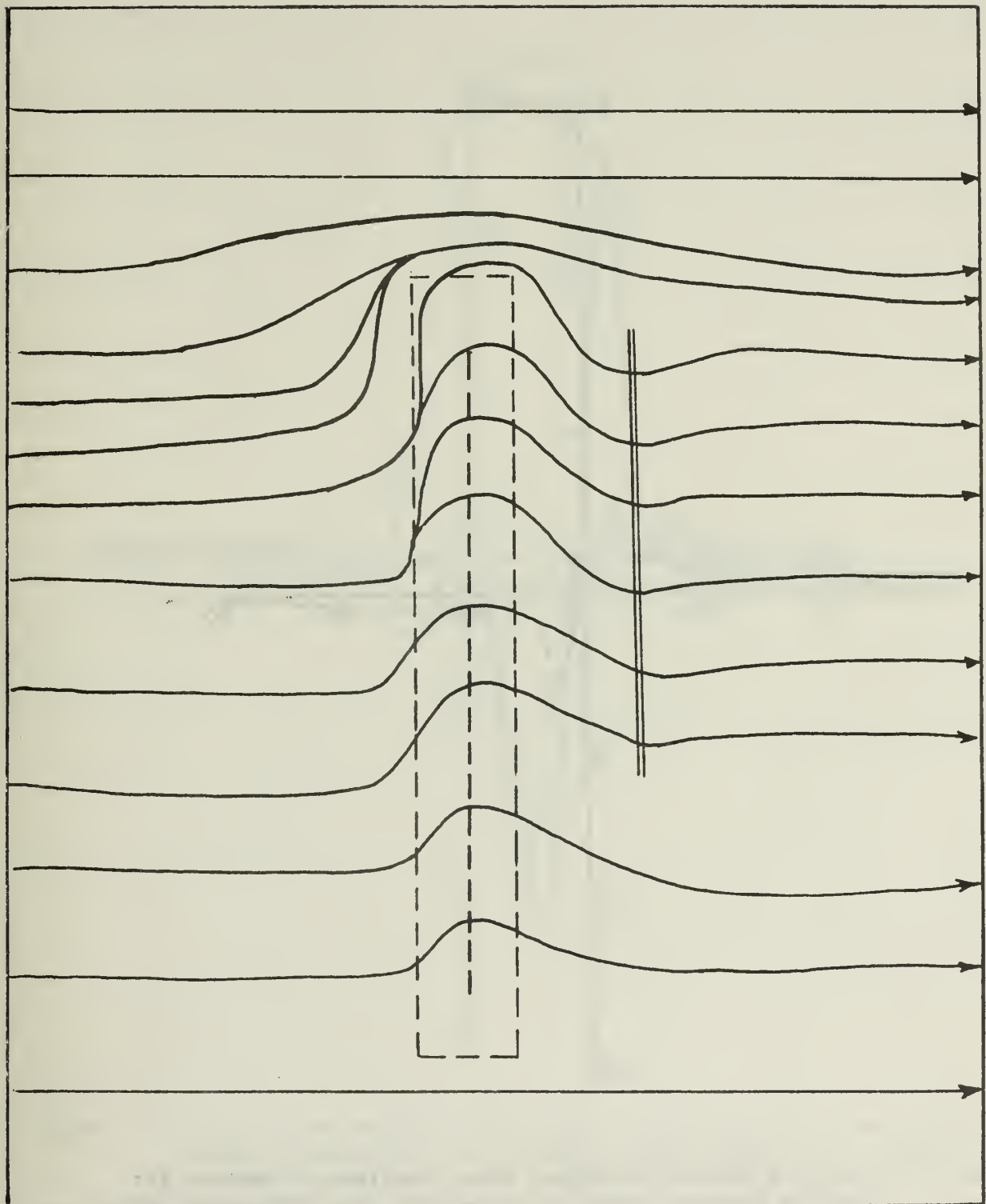


Figure 20.  $3^\circ \times 1.5$  km mountain range case. Six-layer fine resolution model streamlines for  $\sigma = .91667$ .

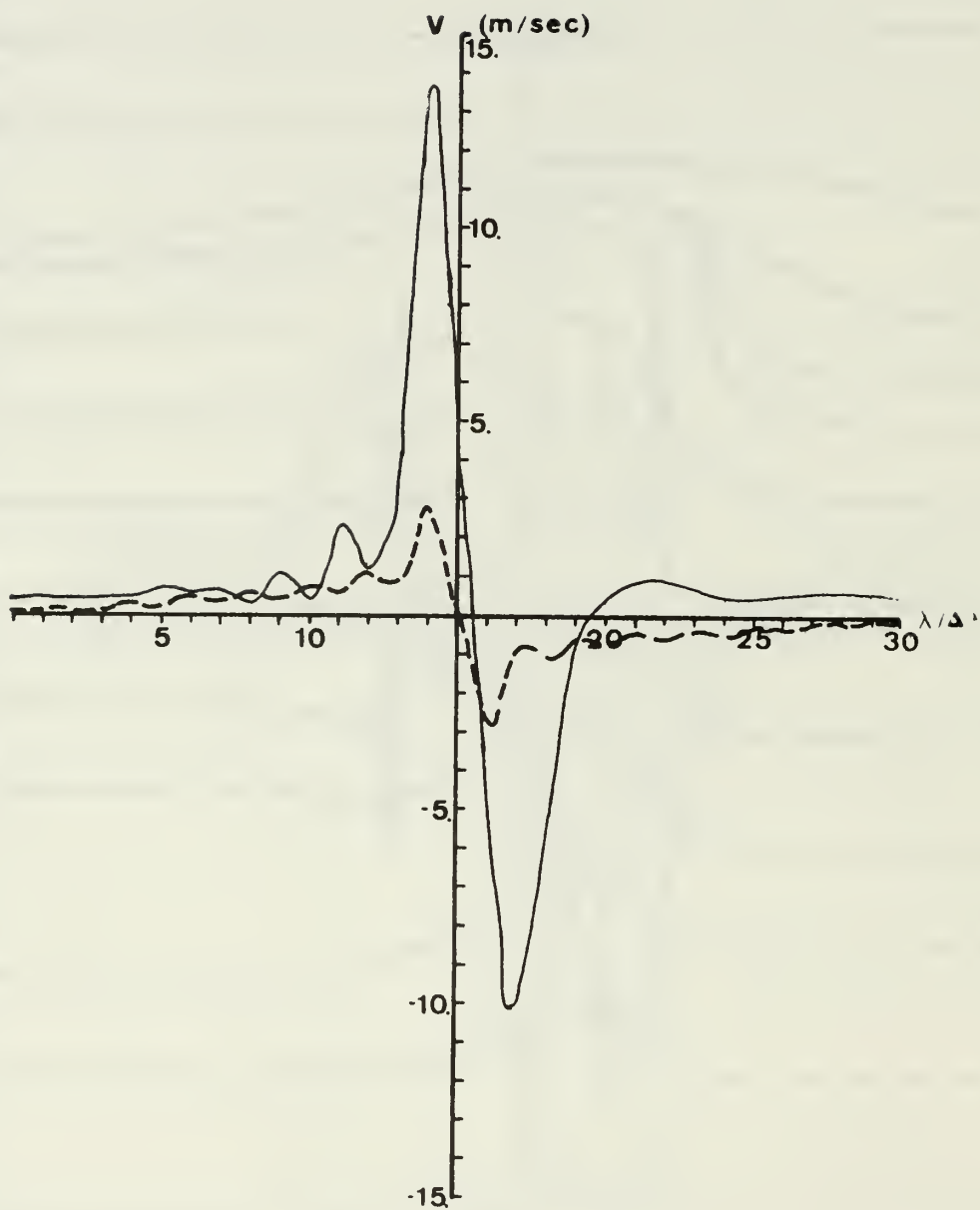


Figure 21.  $3^\circ \times 1.5$  km mountain range case. Analytic  $v$  profile for  $\sigma = 1.0$  (dashed curve) vs. six-layer fine resolution model  $v$  profile for  $\sigma = .91667$  (solid curve) at  $44^\circ\text{N}$ .

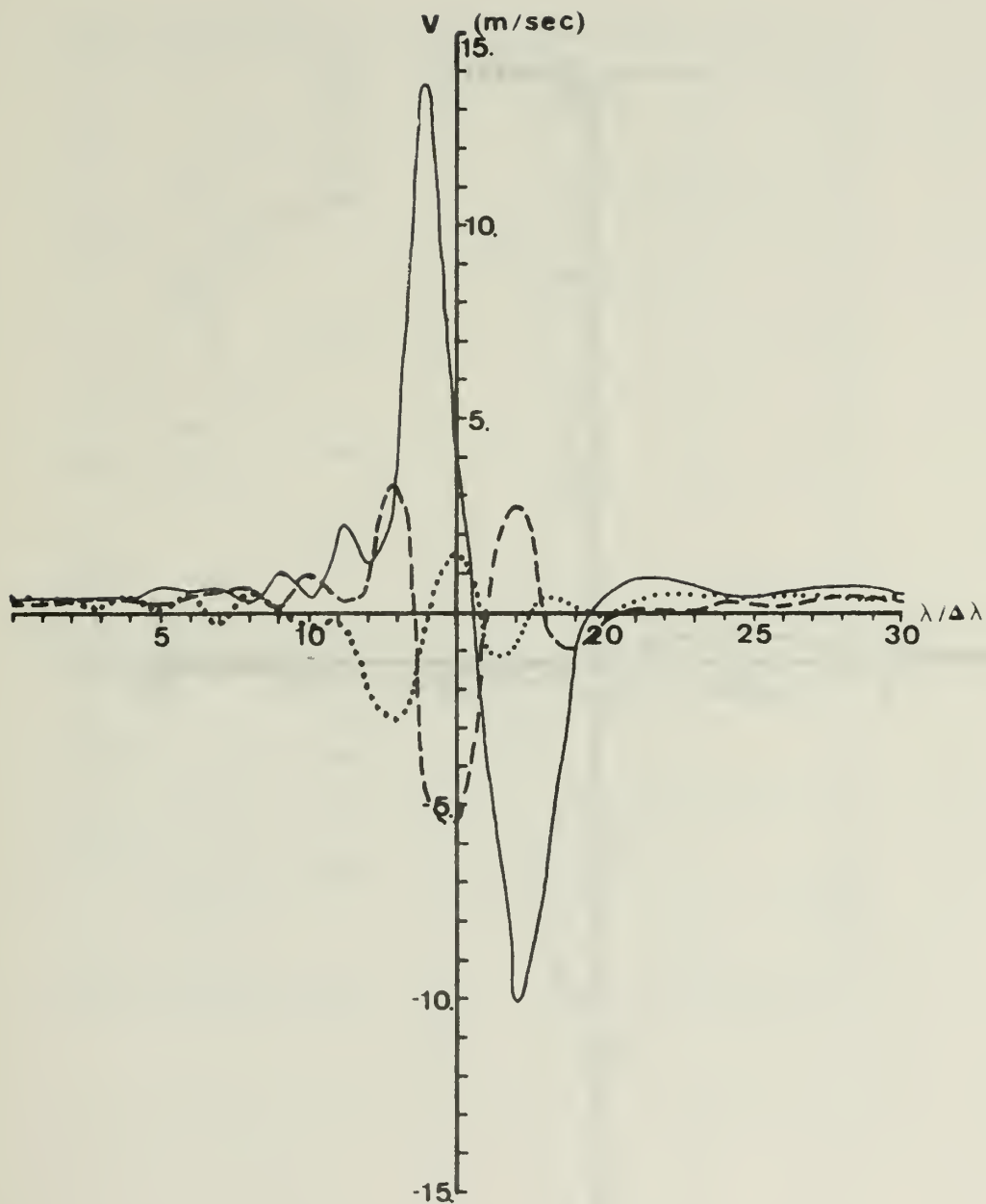


Figure 22.  $3^\circ \times 1.5$  km mountain range case. Six-layer fine resolution model  $v$  profiles for  $\sigma = .91667$  (solid curve),  $\sigma = .58333$  (dashed curve), and  $\sigma = .25$  (dotted curve) at  $44^\circ\text{N}$ .

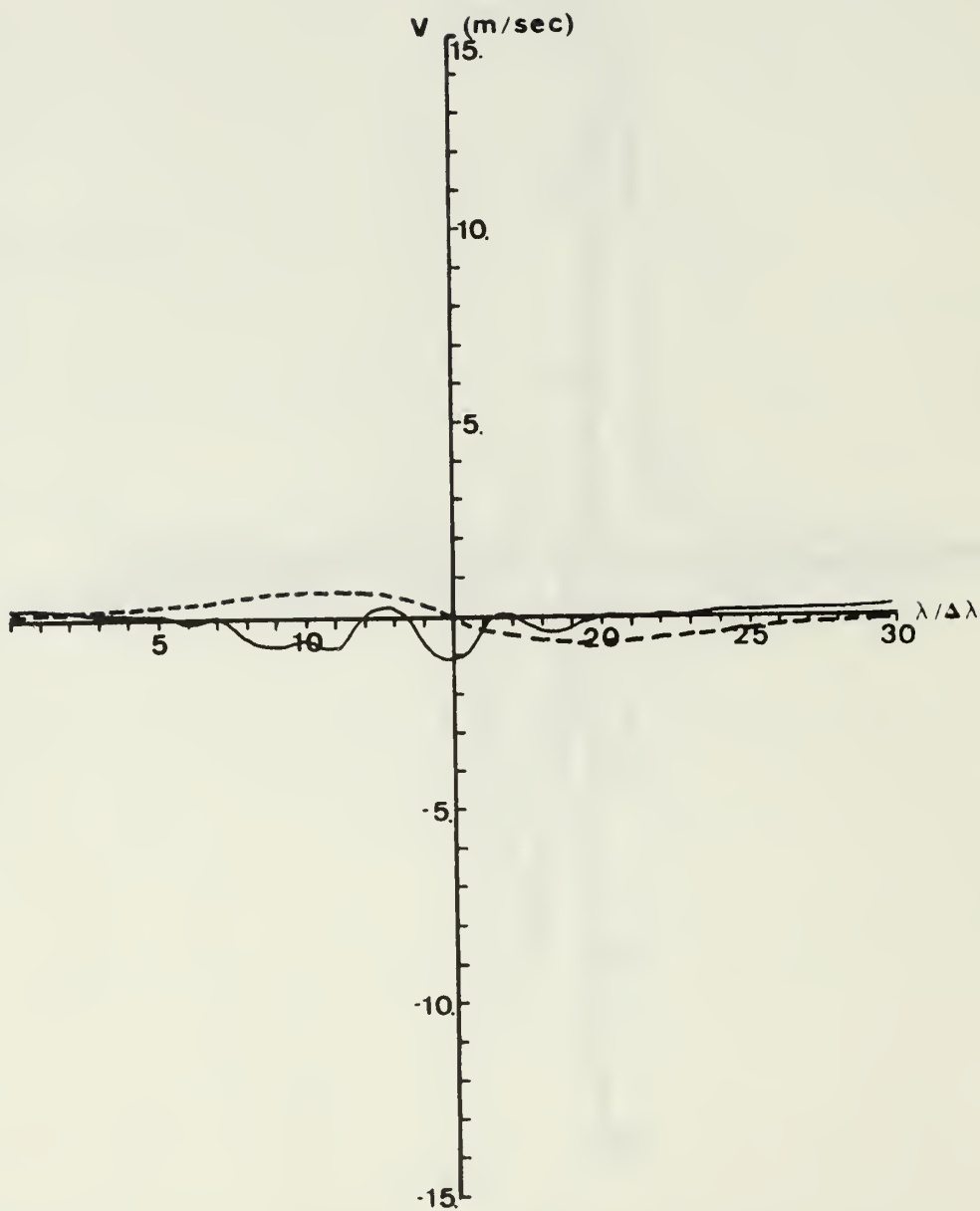


Figure 23.  $3^\circ \times 1.5$  km mountain range case. Analytic  $v$ -profile for  $\sigma = 0$  (dashed curve) vs. six-layer fine resolution model profile for  $\sigma = .08333$  (solid curve). Both at  $44^\circ\text{N}$ .

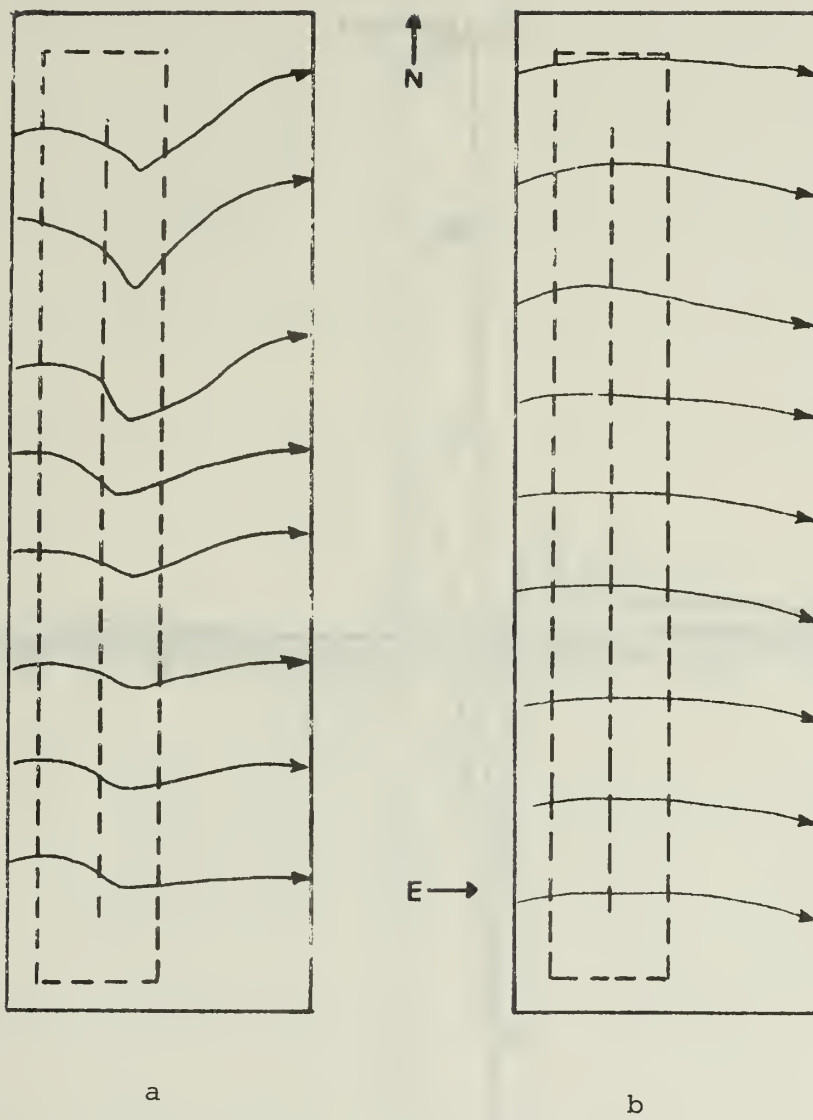


Figure 24.  $3^\circ \times 1.5$  km mountain range case. Streamlines at  $\sigma = .75$   
 from: a. six-layer fine resolution model  
 b. two-layer fine resolution model  
 (dashed lines indicate the topography).

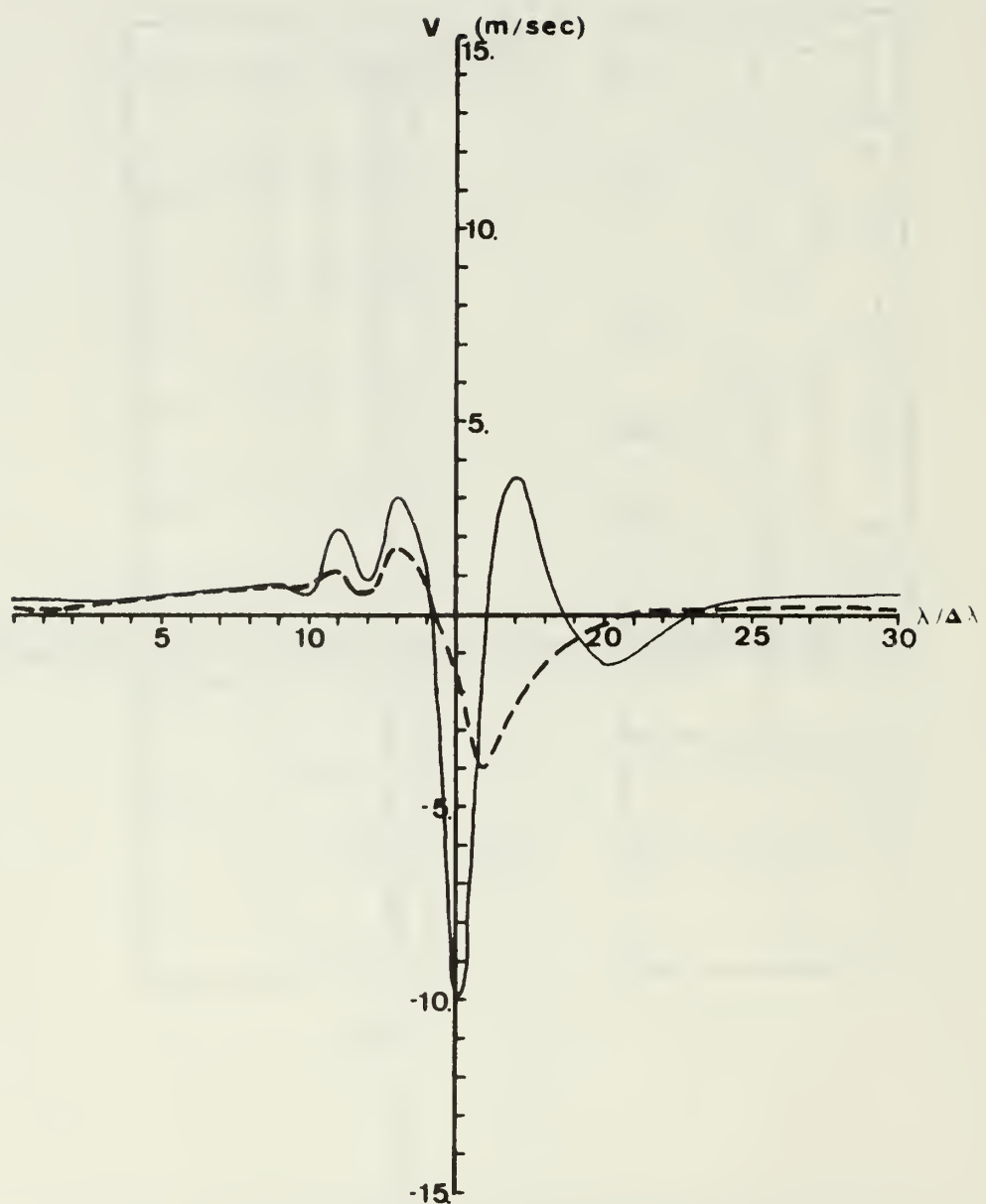


Figure 25.  $3^\circ \times 1.5$  km mountain range case.  $v$ -profiles for  $\sigma = .75$  at  $44^\circ\text{N}$  from six-layer fine resolution model (solid curve) and two-layer fine resolution model (dashed curve).

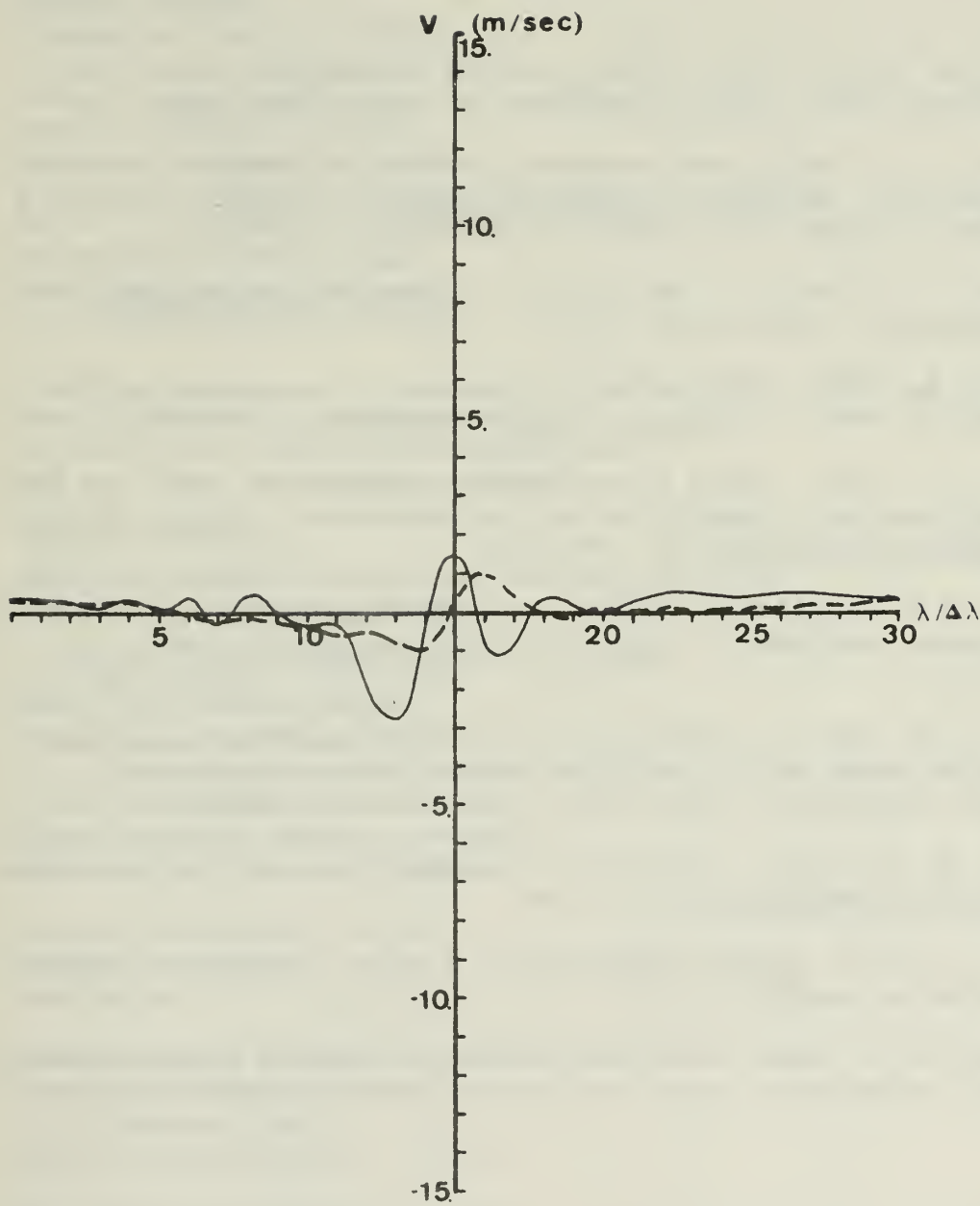


Figure 26.  $3^\circ \times 1.5$  km mountain range case.  $v$  profiles for  $\sigma = .25$  at  $44^\circ\text{N}$  from six-layer fine resolution model (solid curve) and two-layer fine resolution model (dashed curve).

#### LIST OF REFERENCES

- Arakawa, A. and Y. Mintz, 1974: The UCLA General Circulation Model. Workshop Notes, I-VIII, Department of Meteorology, UCLA.
- Charney, J. G., 1967: Some remaining problems in numerical weather prediction. Advances in Numerical Weather Prediction, Travelers Research Center, Inc., Hartford, Connecticut, 61-70.
- Haltiner, G. J. and F. L. Martin, 1957: Dynamical and Physical Meteorology, McGraw-Hill, 52-53.
- Haurwitz, B., 1940: The motion of atmospheric disturbances on the spherical earth. Journal of Marine Research, 3, 254-267.
- Merkine, L., 1975: Steady finite-amplitude baroclinic flow over long topography in a rotating stratified atmosphere. Journal of the Atmospheric Sciences, 32, 1881-1893.
- \_\_\_\_\_, and E. Kalnay-Rivas, 1976: Rotating stratified flow over finite isolated topography. Journal of the Atmospheric Sciences, 33, 908-922.
- Monaco, A. V. and R. T. Williams, 1975: An atmospheric global prediction model using a modified Arakawa differencing scheme. Naval Postgraduate School Report NPS-51Wu75041, 86 pp.
- Neamton, S. M., 1946: The motion of harmonic waves in the atmosphere. Journal of Meteorology, 3, 53-56.
- Queney, P., 1973: Dynamic Meteorology, P. Morel, Editor. D. Riedel Publishing Company, 513-617.
- Williams, R. T., 1976: The polar problem in a global prediction model. Naval Postgraduate School Technical Report NPS-63Wu76111, 29 pp.

## DISTRIBUTION LIST

|   | No. Copies |
|---|------------|
| 1. Defense Documentation Center<br>Cameron Station<br>Alexandria, Virginia 22314  | 2          |
| 2. Library, Code 0142<br>Naval Postgraduate School<br>Monterey, California 93940  | 2          |
| 3. Dr. R. T. Williams, Code 63Wu<br>Department of Meteorology<br>Naval Postgraduate School<br>Monterey, California 93940          | 20         |
| 4. Director<br>Naval Oceanography and Meteorology<br>National Space Technology Laboratories<br>Bay St. Louis, Mississippi 39520   | 1          |
| 5. Officer in Charge<br>Navy Environmental Prediction Research Facility<br>Monterey, California 93940                             | 10         |
| 6. Dean of Research, Code 012<br>Naval Postgraduate School<br>Monterey, California 93940  | 2          |
| 7. Commanding Officer<br>Fleet Numerical Weather Central<br>Monterey, California 93940  | 10         |
| 8. Naval Oceanographic Office<br>Library, Code 3330<br>Washington, D. C. 20373  | 1          |
| 9. AFCRL Research Library<br>ATTN: Nancy Davis/Stop 29<br>L. G. Hanscom Field<br>Bedford, Massachusetts 01730                     | 1          |
| 10. Commander, Air Weather Service<br>Military Airlift Command<br>United States Air Force<br>Scott Air Force Base, Illinois 62226 | 1          |
| 11. Dr. A. Arakawa<br>Department of Meteorology<br>University of California<br>Los Angeles, California 90024                      | 1          |

12. Captain John L. Hayes 10  
Air Force Global Weather Central  
PSC #2  
Box 7141  
Offutt AFB, Nebraska 68113
13. Atmospheric Sciences Library 1  
National Oceanic and Atmospheric Administration  
Silver Spring, Maryland 20910
14. Dr. F. P. Bretherton 1  
National Center for Atmospheric Research  
P. O. Box 3000  
Boulder, Colorado 80303
15. Dr. John Brown 1  
National Meteorological Center/NOAA  
World Weather Building  
Washington, D. C. 20233
16. Dr. C.-P. Chang, Code 63Cj 1  
Department of Meteorology  
Naval Postgraduate School  
Monterey, California 93940
17. Prof. J. G. Charney 1  
54-1424  
Massachusetts Institute of Technology  
Cambridge, Massachusetts 02139
18. Dr. C. Comstock, Code 53Zk 1  
Department of Mathematics  
Naval Postgraduate School  
Monterey, California 93940
19. Dr. Chung-yi Tseng 1  
Atmospheric Physics Div.  
Institute of Physics, Academia Sinica  
Nankang, Taipei 115  
Taiwan, Republic of China
20. Dr. R. L. Elsberry, Code 63Es 1  
Department of Meteorology  
Naval Postgraduate School  
Monterey, California 93940
21. Prof. F. D. Faulkner, Code 53Fa 1  
Naval Postgraduate School  
Monterey, California 93940
22. Captain Harry Hughes 1  
AFIT/CIPF  
Wright-Patterson AFB, Ohio 45433

- |   |   |
|---|---|
| 23. Dr. G. A. Galt<br>NOAA, Pac. Mar. Env. Lab.<br>University of Washington WB-10<br>Seattle, Washington 98105                      | 1 |
| 24. Dr. W. L. Gates<br>Department of Meteorology<br>Oregon State University<br>Corvallis, Oregon 97331                              | 1 |
| 25. Dr. Earl Gossard<br>Wave Propagation Laboratory<br>NOAA/ERL<br>Boulder, Colorado 80302  | 1 |
| 26. Dr. R. Somerville<br>National Center for Atmospheric Research<br>P. O. Box 3000<br>Boulder, Colorado 80303                      | 1 |
| 27. Dr. G. J. Haltiner, Code 63Ha<br>Chairman, Department of Meteorology<br>Naval Postgraduate School<br>Monterey, California 93940 | 1 |
| 28. Dr. R. L. Haney, Code 63Hy<br>Department of Meteorology<br>Naval Postgraduate School<br>Monterey, California 93940              | 1 |
| 29. Lt. D. Hinsman<br>Fleet Numerical Weather Central<br>Monterey, California 93940   | 1 |
| 30. Dr. J. Holton<br>Department of Atmospheric Sciences<br>University of Washington<br>Seattle, Washington 98105                    | 1 |
| 31. Dr. B. J. Hoskins<br>Department of Geophysics<br>University of Reading<br>Reading, United Kingdom                               | 1 |
| 32. Dr. D. Houghton<br>Department of Meteorology<br>University of Wisconsin<br>Madison, Wisconsin 53706                             | 1 |
| 33. Dr. J. Wallace<br>Department of Atmospheric Sciences<br>University of Washington<br>Seattle, Washington 98105                   | 1 |

34. Dr. J. Young 1  
Department of Meteorology  
University of Wisconsin  
Madison, Wisconsin 53706
35. Dr. S. K. Kao 1  
Department of Meteorology  
University of Utah  
Salt Lake City, Utah 84112
36. Dr. A. Kasahara 1  
National Center for Atmospheric Research  
P. O. Box 3000  
Boulder, Colorado 80303
37. Dr. M. G. Wurtele 1  
Department of Meteorology  
University of California  
Los Angeles, California 90024
38. Cdr. W. R. Lambertson 1  
Fleet Weather Facility Suitland  
Navy Department  
Washington, D. C. 20373
39. Dr. C. E. Leith 1  
National Center for Atmospheric Research  
P. O. Box 3000  
Boulder, Colorado 80303
40. Dr. J. M. Lewis 1  
Laboratory for Atmospheric Research  
University of Illinois  
Urbana, Illinois 61801
41. Dr. E. N. Lorenz 1  
Department of Meteorology  
Massachusetts Institute of Technology  
Cambridge, Massachusetts 02139
42. Lt. Olaf M. Lubeck 1  
Department of Meteorology  
Naval Postgraduate School  
Monterey, California 93940
43. Dr. R. Madala 1  
Code 7750  
Naval Research Laboratories  
Washington, D. C. 20390
44. Dr. J. D. Mahlman 1  
Geophysical Fluid Dynamics Laboratory  
Princeton University  
Princeton, New Jersey 08540

45. Meteorology Library, Code 63  
Naval Postgraduate School  
Monterey, California 93940 1
46. National Center for Atmospheric Research  
Box 1470  
Boulder, Colorado 80302 1
47. Director, Naval Research Laboratory  
ATTN: Technical Services Information Center  
Washington, D. C. 20390 1
48. Dr. E. C. Nickerson  
NOAA, Atmospheric Physics & Chemistry Laboratory  
Boulder, Colorado 80302 1
49. Department of Oceanography, Code 68  
Naval Postgraduate School  
Monterey, California 93940 1
50. Office of Naval Research  
Department of the Navy  
Washington, D.C. 20360 1
51. Dr. T. Ogura  
Laboratory for Atmospheric Research  
University of Illinois  
Urbana, Illinois 61801 1
52. Prof. K. Ooyama  
National Center for Atmospheric Research  
P. O. Box 3000  
Boulder, Colorado 80303 1
53. Dr. I. Orlanski  
Geophysical Fluid Dynamics Laboratory  
Princeton University  
Princeton, New Jersey 08540 1
54. Prof. N. A. Phillips  
National Meteorological Center/NOAA  
World Weather Building  
Washington, D. C. 20233 1
55. Dr. S. Piacsek  
Code 7750  
Naval Research Laboratory  
Washington, D. C. 20390 1
56. Dr. J. Smagorinsky, Director  
Geophysical Fluid Dynamics Laboratory  
Princeton University  
Princeton, New Jersey 08540 1

57. Dr. T. Rosmond 1  
Navy Environmental Prediction Research Facility  
Monterey, California 93940
58. Dr. D. Williamson 1  
National Center for Atmospheric Research  
P. O. Box 3000  
Boulder, Colorado 80303
59. Dr. Y. Sasaki 1  
Navy Environmental Prediction Research Facility  
Monterey, California 93940
60. Prof. A. L. Schoenstadt 1  
Code 53Zh  
Naval Postgraduate School  
Monterey, California 93940
61. Dr. Fred Shuman, Director 1  
National Meteorological Center  
World Weather Building  
Washington, D. C. 20233
62. Dr. Joanne Simpson 1  
Department of Environmental Sciences  
2015 Ivy Road  
Charlottesville, Virginia 22903
63. Professor Fedor Mesinger 1  
Department of Meteorology  
University of Belgrade  
11001 Beograd, p.p.550  
Yugoslavia

U178579

DUDLEY KNOX LIBRARY - RESEARCH REPORTS



5 6853 01071311 8

U178579

NP